nature geoscience

Article

https://doi.org/10.1038/s41561-025-01894-y

Amplified Arctic–boreal fire regimes from permafrost thaw feedbacks

Received: 12 November 2024

Accepted: 26 November 2025

Published online: 09 January 2026

Check for updates

Jialing Li[1,2,12], Gengke Lai[2,12], Lin Meng[3], Constantin M. Zohner[4], Josep Peñuelas[5,6], Sander Veraverbeke[7], Jan Hjort[8], Philippe Ciais[9], Yang Chen[10], Xin Li[11] & Chaoyang Wu[1]

Widespread permafrost thaw—indicated by the thickening of the soil active layer, which undergoes seasonal freeze–thaw cycles above the permafrost—has important implications for the thermal, hydrological and ecological processes of Arctic–boreal ecosystems. Yet, how thaw-driven biophysical and ecological feedbacks alter Arctic–boreal fire regimes remains poorly understood. Here we quantify these feedbacks by integrating long-term observations of soil active layer thickness (1997–2018) with a causal inference model and a space-for-time approach. We show that the thickening of the soil active layer can amplify summer fire regimes across the Arctic–boreal region, resulting in intensified fire weather conditions, increased burned area and higher fire emissions. The fire amplifications were driven by thaw-induced reductions in surface albedo and soil moisture that intensify summer warming and atmospheric aridity, further reinforced by enhanced vegetation growth and the desiccation of soil organic matter. These cascading feedbacks may create a positive fire–climate feedback loop, whereby more burning accelerates carbon release from vegetation and soil, further destabilizing northern ecosystems. Our findings highlight the potential escalating fire and climate risks initiated by permafrost thaw, emphasizing the urgent need for immediate climatic action to mitigate climate change and the compounding impacts of wildfires and permafrost degradation.

Permafrost is one of the largest terrestrial carbon pools, storing vast amounts of organic carbon that have remained frozen for millennia[1,2]. However, ongoing climatic warming and Arctic amplification are driving rapid permafrost thaw, which mobilizes stored carbon, amplifies carbon–climate feedbacks and undermines infrastructure[3–6]. Thawing also deepens the active layer thickness (ALT)—the soil layer above permafrost that undergoes seasonal freeze–thaw cycles[7,8]. The active layer plays a vital role in cold ecosystems, as it regulates most ecological, hydrological and biochemical processes[9]. Disturbances such as wildfires further accelerate permafrost thaw by altering the soil thermal regime[10–13]. Permafrost thaw can, in turn, feed back to climate and landscape by reshaping thermal, hydrological and vegetation regimes[14–16]. Yet, despite their profound implications, the feedback mechanisms of permafrost thaw on Arctic–boreal wildfires remain poorly understood.

Wildfires have recently increased in size and severity in several high-latitude permafrost regions owing to warmer and drier conditions[17,18]. Wildfires depend on multiple factors such as fuel availability and dryness, ignition sources and favorable meteorological conditions[19]. Permafrost thawing, initiated by climate change, may exacerbate these conditions, making northern landscapes increasingly vulnerable to fire. Previous studies, largely based on Earth system model simulations, have primarily focused on the biophysical feedbacks of permafrost thaw to local climate, such as reductions in soil moisture and relative humidity and increases in near-surface

A full list of affiliations appears at the end of the paper. e-mail: wucy@igsnrr.ac.cn

temperature, convective precipitation and lightning, highlighting their potential in intensifying wildfire risk[20,21]. However, much less attention has been paid on how permafrost thaw alters vegetation dynamics and desiccation of surface organic matter, both of which critically determine the amount and flammability of available fuels. The active layer constitutes the rooting zone, where thawing may increase nutrient availability[22], facilitating the establishment of more trees in boreal forests[23] and the expansion of shrubs in the Arctic tundra[24]. At the same time, boreal forest and tundra hold large reservoirs of soil organic carbon (SOC)[25], which accounts for 66–79% of fuel consumed during wildfires[26]. The drying of surface and below-ground organic layers may therefore represent an overlooked but essential pathway linking thaw to Arctic–boreal fires[13,27]. Despite these findings, the combined impacts of permafrost thaw on Arctic–boreal fire regimes—through both climatic feedbacks and fuel-related mechanisms—remain poorly understood and largely unquantified.

The complex bidirectional interactions between permafrost dynamics and climate variability make it challenging to identify and isolate the feedbacks resulting from permafrost thaw[7,20]. Earth system models provide a valuable platform to explore these feedbacks through controlled simulations[20,21], but they are limited by the incomplete representations of key biophysical and biological processes and often lack an explicit treatment of permafrost dynamics[3]. The increasing availability of observational data, from both field measurements and satellite products, may contribute to an improved understanding of permafrost thaw feedbacks across spatiotemporal scales. However, observational evidence remains limited. Moreover, traditional statistical approaches (for example, correlation and regression) have limitations in uncovering causal associations between variables[28] and are prone to bias when dealing with complex bidirectional systems[29,30]. By contrast, convergent cross mapping (CCM), a causal inference model, can discover both unidirectional and bidirectional causal links between variables over time[31]. Moreover, the space-for-time (SFT) approach, widely used to detect climate feedbacks from vegetation dynamics[29] and land-cover changes[32], has the capability to disentangle unidirectional feedbacks from complex bidirectional associations[29]. Therefore, integrating CCM and SFT approaches can help to quantify the feedback effects from permafrost thaw on climate and landscape from observational data.

Here, we hypothesized that permafrost thaw, indicated by a deepening ALT, alters fire regimes across the northern permafrost zone (>45° N). To test this, we combined the CCM model and SFT approach to quantify the biophysical and biological feedbacks of increasing ALT on summer (June–August) climatic conditions, vegetation growth and below-ground fuel dryness. The CCM identifies the directional influence between variables in complex dynamical systems using non-linear state space reconstruction. The CCM tests causality by assessing whether the reconstructed states of one variable can reliably predict those of another, with predictive skill measured by the cross-mapping coefficients (ρ). The evidence for directional influence is inferred when ρ increases and converges as the length of the time series (L) increases. To assess convergence, we calculated the Spearman's rank correlation between ρ and L and considered causal influence present only when the correlation was significantly positive[33] (Methods and Extended Data Fig. 1). The SFT approach compared changes in multiple factors between pixels experiencing permafrost thaw and their neighbouring pixels with similar background climate trends under specific constraints. By comparing the thawing pixels to closely matched controls, this approach isolates the effects of permafrost thaw from broader climatic variability (Methods and Extended Data Fig. 2). These analyses were based on hemispheric ALT data from the European Space Agency (ESA) permafrost product (version 3.0) from 1997 to 2018. We further provided conservative, lower-bound quantifications of the impacts of deepening ALT on Arctic–boreal fire regimes, including changes in fire weather conditions, burned area and resultant fire emissions. The uncertainty propagation was incorporated throughout the estimations of fire regime changes using Monte Carlo simulations (Methods and Extended Data Fig. 3).

Deeper ALT drives intensified meteorological drought

The long-term ESA hemispheric ALT products indicated a widespread deepening ALT across the northern permafrost zone, with significantly increasing trends in approximately 56.4% of the areas compared with only 1.5% showing decreasing trends during 1997–2018 ($P < 0.05$, Fig. 1a). The thickening trends were stronger in areas of continuous permafrost in northeastern Siberia and northwestern North America and in isolated and sporadic areas near the southern edge of permafrost. ALT ground measurements from the Circumpolar Active Layer Monitoring (CALM) observational network (Supplementary Fig. 1), together with the hemispheric ALT product extending to 2021 (Supplementary Fig. 2), consistently indicated a progressive increase in ALT.

We found evidence that this widespread deepening of ALT triggers biophysical feedbacks to the local climate, creating fire-prone meteorological conditions. A causal analysis using the CCM model revealed that ALT exerted a causal influence on summer vapour pressure deficit (VPD), a direct measure of atmospheric dryness. Across 63.1% of permafrost regions ($P < 0.05$; Fig. 1b), ρ showed a significant positive convergence with L, indicating that the variability in ALT reliably predicts variations in VPD. This causality was further supported by ALT ground measurements from the CALM observational network (Extended Data Fig. 4a) and by multivariate CCM, which showed that the causal effect of ALT on VPD was strengthened after removing the confounding influence of rising temperature (Supplementary Fig. 3). A causal linkage was also identified between ALT and climatic water deficit (CWD; Supplementary Fig. 4a), a measure of water balance deficit that can characterize plant water stress and fuel dryness[34].

We further applied the SFT approach to quantify the sensitivity of summer VPD to ALT change. Over the 22-year period, most permafrost areas (69.2%) showed a positive sensitivity, suggesting that VPD tends to increase with deepening ALT (Fig. 1c). This effect was particularly pronounced in areas with continuous permafrost, where VPD increased by 0.011 kPa for every 1 cm increase in ALT (Extended Data Fig. 5). The results remained consistent when using the hemispheric ALT product extending to 2021 (Supplementary Fig. 5). Moreover, a deepening of ALT could increase CWD across most areas (68.2%; Supplementary Fig. 4b). We further investigated the biophysical mechanisms underlying the relationship between deepening ALT and intensified summer meteorological drought. This relationship could be mediated by several variables. The sensitivity estimates based on the SFT approach revealed that deepening ALT reduced surface albedo in 58.2% of regions, which subsequently led to increased air temperature in 71.4% of regions and decreased relative humidity in 65.1% of regions, both contributing to the rise in VPD (Fig. 1d–f). These biophysical feedbacks were more pronounced in areas with continuous permafrost (Extended Data Fig. 5).

Deeper ALT drives vegetation growth and fuel dryness

Fuel availability and dryness play essential roles in driving Arctic–boreal wildfires. We therefore assess the impacts of permafrost thaw on vegetation growth, indicated by summer fractional vegetation coverage (FVC). The CCM model applied to both hemispheric ALT data and CALM sites indicated a directional influence of ALT on FVC (Fig. 2a and Extended Data Fig. 4b). Consistent with this, the SFT approach revealed a positive sensitivity of FVC to ALT across 60.3% of permafrost regions, indicating that FVC tends to increase with deepening ALT (Fig. 2e). Moreover, deepening ALT was found to causally increase leaf area index (LAI; Extended Data Fig. 4c,d and Supplementary Fig. 4c,d). These increases in FVC and LAI suggest that the permafrost thaw increases the

https://doi.org/10.1038/s41561-025-01894-y

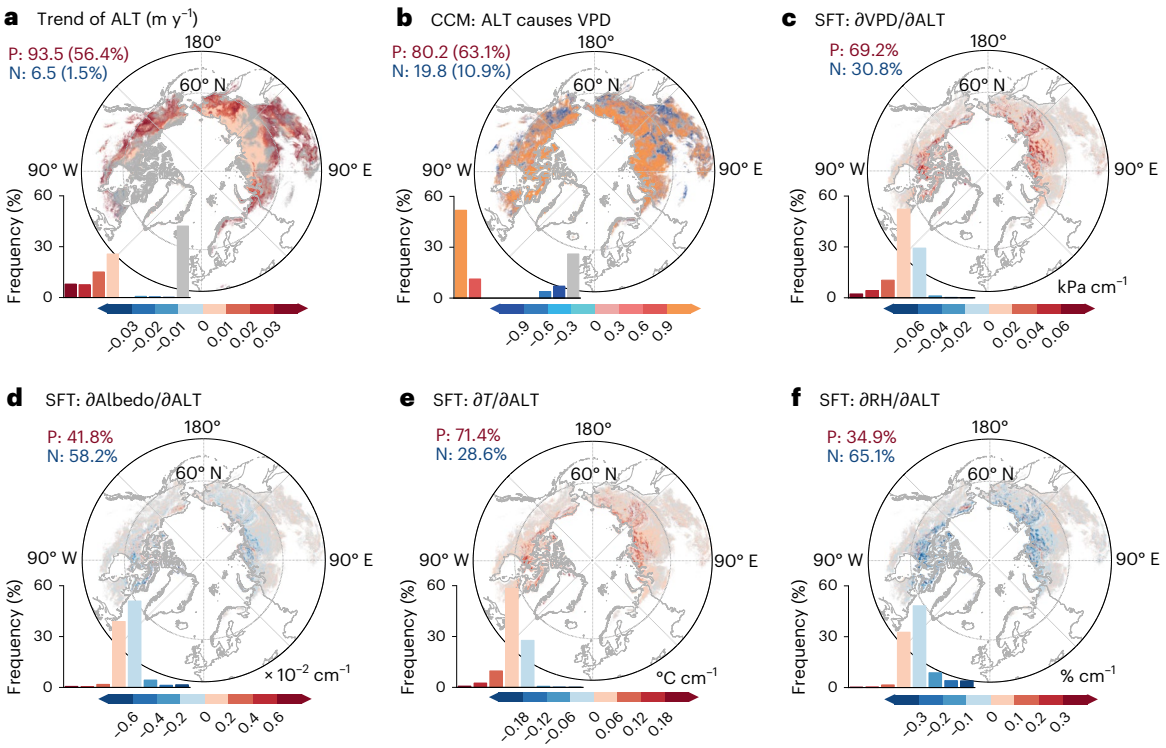

Fig. 1 | Climatic feedbacks from deepening ALT on amplified summer meteorological drought conditions across the northern permafrost zone (>45° N). a, Long-term ALT trends spanning 1997–2018. **b**, A causal analysis using the CCM model to establish the causal link of 'ALT causes VPD'. The map displays Spearman's rank correlations between ρ and L estimated by the CCM model. The colour bar in **b** denotes Spearman's correlation between ρ and L. **c**–**f**, The overall sensitivities of summer VPD (∂VPD/∂ALT) (**c**), albedo (∂Albedo/∂ALT) (**d**), air temperature (∂T/∂ALT) (**e**) and relative humidity (∂RH/∂ALT) (**f**) to changes in ALT. P and N indicate the percentages of positive and negative correlations or sensitivities, respectively. The overall sensitivities were calculated by averaging the annual sensitivities from 1997 to 2018 derived from the SFT approach (Methods). Maps created with ArcGIS (v.10.8) using basemap data from the IPCC-WG1 Atlas GitHub repository[80].

biomass, coverage and spatial connectivity of above-ground vegetation, thereby enhancing fuel availability and continuity.

The litter in the top soil and below-ground SOC are primary fuel sources in boreal forest and tundra fires, whose dryness critically influences fire behaviour and combustion emissions[26]. We therefore additionally investigated the potential effect of permafrost thaw on below-ground fuel dryness, indicated by the fine fuel moisture code (FFMC) for surface litter (top 1–2 cm), the duff moisture code (DMC) for the duff layer at a depth of 5–10 cm and the drought code (DC) for the deeper compact organic layer (10–20 cm). Using the CCM model, we found that deepening ALT had causal impacts on FFMC, DMC and DC, as indicated by both hemispheric ALT data (Fig. 2b–d) and ALT measurements from the CALM sites (Extended Data Fig. 4d–f). The results from the SFT approach showed positive sensitivities of FFMC, DMC and DC to increased ALT across the majority of permafrost regions (58.5%, 61.4% and 60.4%, respectively), suggesting that the thickened ALT led to drier fuels in different soil layers (Fig. 2f–h). In summary, permafrost thaw could alter above-ground biological and below-ground hydrological processes, leading to the enhancement of vegetation growth and underground fuel dryness. These amplifying effects were more pronounced in areas of continuous permafrost (Extended Data Fig. 5).

Arctic–boreal fire regime changes due to deeper ALT

The above permafrost thaw feedbacks may alter Arctic–boreal fire regimes. We provided a preliminary quantification of changes in summer fire regimes driven by deepening ALT, including fire weather index (FWI), burned area and fire emissions. Using XGBoost models for four fire regions from the Global Fire Emissions Database (GFED; Supplementary Fig. 6), we simulated variations in summer FWI as a function of changes in air temperature, VPD and relative humidity, achieving a high accuracy (R^2 of 0.82–0.95; Extended Data Fig. 6). The ALT increased by 24.3 cm on average across the northern permafrost zone during 1997–2018, contributing to higher air temperature (+0.19 °C), elevated VPD (+0.08 kPa) and reduced relative humidity (−0.41%) (Fig. 3a–d, Extended Data Fig. 7 and Supplementary Table 1). On the basis of the XGBoost FWI models, these atmospheric changes raised summer FWI by 0.14 ± 0.02 (Fig. 3e), corresponding to 16.1% of FWI increases over the study period (Supplementary Fig. 7). Notably, the permafrost thaw-associated increase in FWI was strongest at high latitudes, particularly north of the Arctic Circle, where local increases reached values up to 13 (Fig. 3e).

We further applied a cubic function to model the non-linear relationship between changes in summer total burned area and changes in summer FWI (Methods and Extended Data Fig. 8). The thaw-induced higher FWI contributed to an additional 6.87 ± 5.30 Mha of summer burned area across the northern permafrost zone during 1997–2018, with the largest impacts observed in Siberia and northwestern North America (Fig. 3f,i). Increased fire activity in carbon-rich ecosystems may increase carbon release into the atmosphere. We used a bottom-up approach to estimate the additional fire emissions (primarily CO_2 and CH_4) resulting from increased burned area. The estimation integrated two sources of fuel consumption data (GFED4.1s and a high-resolution 500-m data; Supplementary Fig. 8), contributions of different fire types (Supplementary Fig. 9) and emission factors (Methods and Supplementary Table 2). Our results indicated that deepening ALT has elevated fire emissions across the northern permafrost zone, particularly in Siberia and northwestern North America (Fig. 3g,h).

https://doi.org/10.1038/s41561-025-01894-y

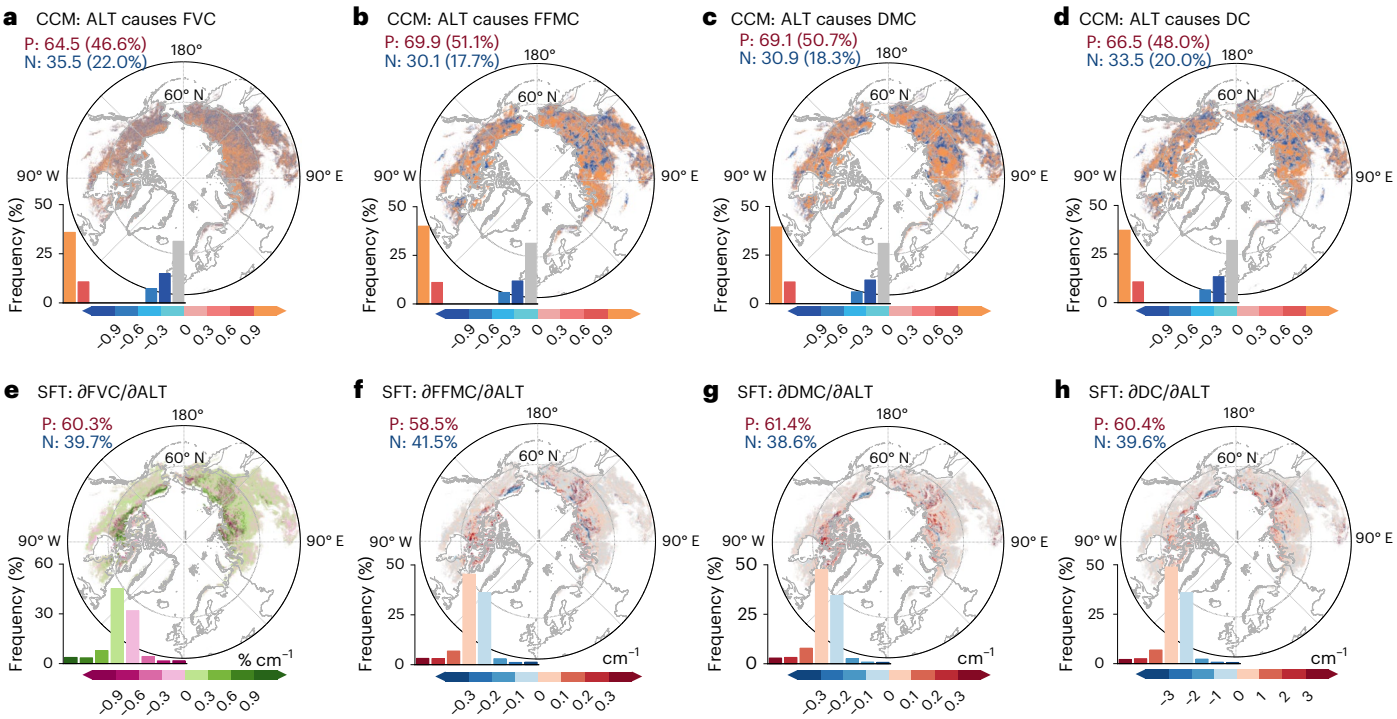

Fig. 2 | Feedbacks from deepening ALT on vegetation growth and below-ground fuel dryness across the northern permafrost zone (>45° N). **a**–**d**, Causal analyses using the CCM model to establish the causal links of 'ALT causes FVC' (**a**), 'ALT causes FFMC' (**b**), 'ALT causes DMC' (**c**) and 'ALT causes DC' (**d**). The maps display Spearman's rank correlation coefficient between predictive skill (ρ) and the length of the time series (L) estimated by the CCM model. The colour bars in **a**–**d** denote Spearman's correlation between ρ and L. **e**–**h**, Overall sensitivities of summer FVC (∂FVC/∂ALT) (**e**), FFMC (∂FFMC/∂ALT) (**f**), DMC (∂DMC/∂ALT) (**g**) and DC (∂DC/∂ALT) (**h**) to changes in ALT. P and N indicate the percentages of positive and negative correlations or sensitivities, respectively. Maps created with ArcGIS (v.10.8) using basemap data from the IPCC-WG1 Atlas GitHub repository[80].

Using the GFED4.1s-derived fuel consumption, we estimated that total fire emissions increased by 275.87 ± 275.74 Tg CO_2e from 1997 to 2018, primarily from CO_2 (250.22 ± 249.78 Tg CO_2e), with the remainder from CH_4 (25.65 ± 31.00 Tg CO_2e) (Fig. 3i and Extended Data Fig. 9a,b). The higher fuel consumption in the 500-m data yielded a roughly 1.6-fold increase in total fire emissions (433.37 ± 416.49 Tg CO_2e), consisting mainly of CO_2 (393.29 ± 377.53 Tg CO_2e) and CH_4 (40.08 ± 46.16 Tg CO_2e) (Fig. 3i and Extended Data Fig. 9c,d). The largest emission increases occurred in regions with continuous permafrost (152.53 ± 148.01 Tg CO_2e for GFED4.1s and 256.61 ± 227.53 Tg CO_2e for the 500-m data; Fig. 3g,h), where ALT-induced increases in burned area were most pronounced (Fig. 3f), affecting extensive areas of boreal forest and peatland (Supplementary Figs. 8 and 9).

Thaw-induced fire–climate feedbacks and ecosystem impacts

Our findings revealed that permafrost thaw could trigger multiple biophysical and biological feedbacks that intensify summer meteorological drought, promote vegetation growth and exacerbate below-ground fuel dryness, potentially leading to increased Arctic–boreal fire activity and emissions (Fig. 4). We developed a structural equation model (SEM) to identify the underlying mechanisms and causal connections among these feedback processes. Three main pathways were identified: surface soil moisture content (pathway A), FVC (pathway B) and below-ground fuel dryness (pathway C) (Extended Data Fig. 10).

Deepening ALT intensified the summer meteorological drought by increasing near-surface air temperatures, primarily through changes in surface energy balance. Specifically, ALT deepening reduced surface albedo, probably owing to enhanced vegetation growth following permafrost thaw (pathway B). The increased vegetation cover decreases the reflection of shortwave radiation and increases the longwave emission from the land surface, thereby warming the lower atmosphere. This finding is consistent with evidence linking vegetation shifts to the Arctic–boreal albedo feeback[16,23,35]. In addition to these radiative effects, reduced surface soil moisture in response to deeper thaw promotes greater sensible heat fluxes to the atmosphere (pathway A), a mechanism supported by regional climate model simulations[20]. Moreover, the direct release of greenhouse gases (for example, CO_2 and CH_4) from permafrost thaw reinforces this regional warming[1,3,4] (Fig. 4). Thaw-induced surface drying also led to lower relative humidity, aligning with climate model simulations[20]. Together, these warmer and drier atmospheric conditions amplify fire weather, increasing the likelihood and severity of wildfires.

Permafrost thaw can also alter vegetation dynamics, promoting boreal forest expansion and tundra shrubification[23,24,36] (Fig. 4 and pathway B). The active layer is critical for northern vegetation dynamics, as it serves as the rooting zone from which plants can absorb soil nutrients and water during summer[22,37]. The permafrost thaw enhances the water downward infiltration into the root zone, promoting tree growth by increasing water availability[38,39]. The thickness of the active layer also determines the proportion of mineral organic carbon that is either accessible or locked in permafrost[40]. The microbial decomposition of soil organic matter may accelerate as ALT deepens and temperatures rise, increasing soil nutrient availability and thereby promoting plant growth[14,40]. The landscape microtopography and ice content of permafrost also probably play a crucial role in determining vegetation changes[14]. For example, the gradual thawing of ice-poor permafrost on sloped, well-drained terrain can enhance vegetation productivity and facilitate the establishment of shrubs[14], which are more fire-tolerant and can sustain a higher frequency of fire[41].

In addition, our results show intensified below-ground fuel dryness, probably driven by reduced surface soil moisture from

https://doi.org/10.1038/s41561-025-01894-y

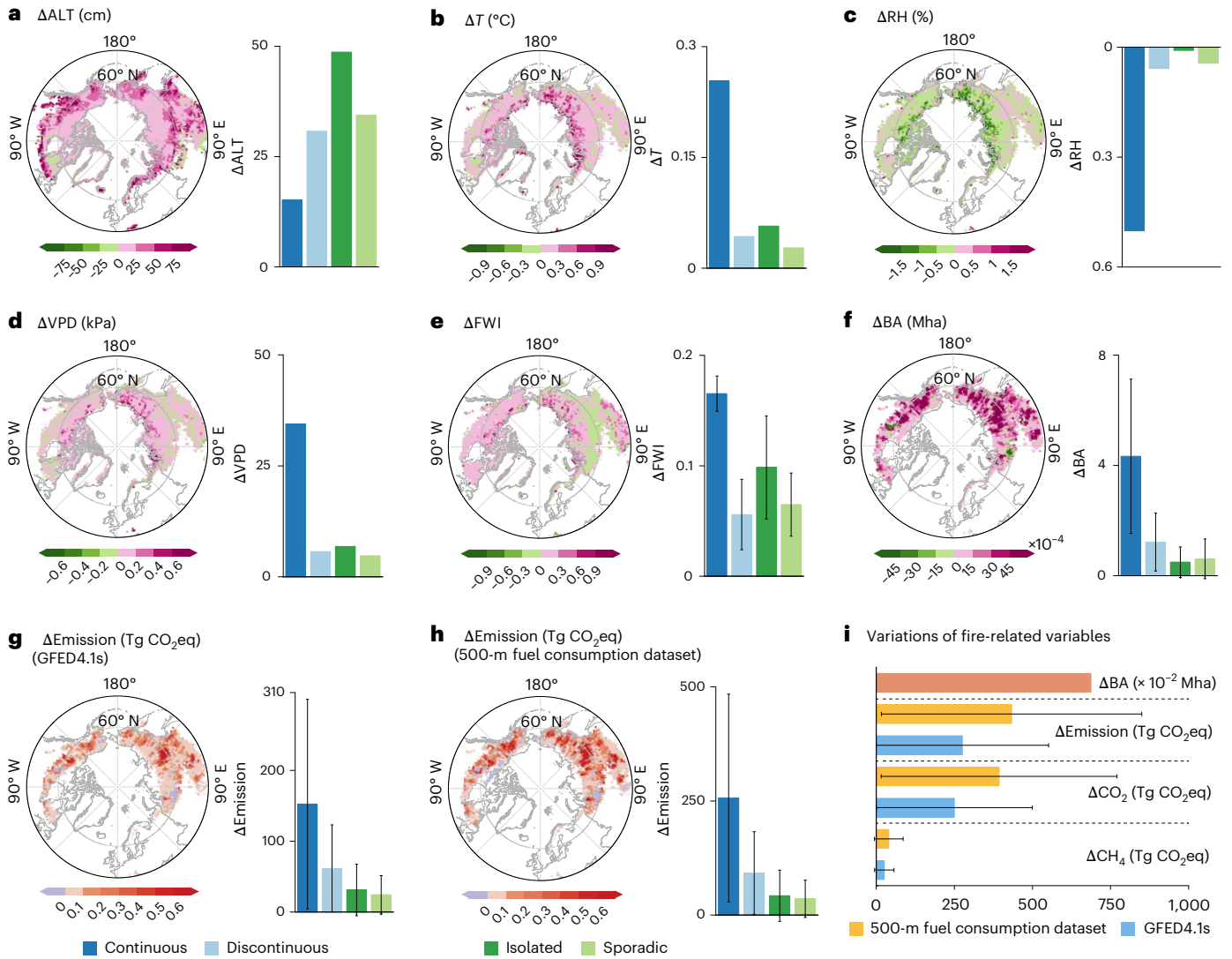

Fig. 3 | Changes in fire weather, burned area and fire emission induced by deepening ALT over 1997–2018. a–**f**, Changes in ALT (ΔALT, **a**) over 1997–2018 and their induced changes in summer air temperature (Δ*T*, **b**), relative humidity (ΔRH, **c**), VPD (ΔVPD) (**d**), FWI (ΔFWI) (**e**), burned area (ΔBA) (**f**) and fire emissions (ΔEmission including ΔCO_2 and ΔCH_4) (**g**,**h**); changes in fire emissions were calculated based on a bottom-up model using the GFED4.1s (**g**) and the 500-m fuel consumption datasets (**h**), respectively. **i**, The bars and error bars are presented as mean values ± 1 s.d. of regional sums of ΔBA, ΔEmission, ΔCO_2 and ΔCH_4 for the northern permafrost zone derived from 10,000 Monte Carlo simulations. The bars in **a**–**d** represent the regional average changes across different permafrost types (continuous, $n = 2{,}319$; discontinuous, $n = 518$; isolated, $n = 338$; and sporadic, $n = 431$). The bars and error bars in **e** are presented as mean values ± 1 s.d. of regional average of ΔFWI for each permafrost type derived from 10,000 bootstrapped XGBoost model runs. The bars and error bars in **f**–**h** are presented as mean values ± 1 s.d. of regional sums of ΔBA and ΔEmission for each permafrost type derived from 10,000 Monte Carlo simulations. Maps created with ArcGIS (v.10.8) using basemap data from the IPCC-WG1 Atlas GitHub repository[80].

permafrost thaw (pathway C). This process desiccates surface litter (higher FFMC) and organic material in deeper soil layers (higher DMC and DC). Given the abundance of soil organic material, which constitutes much of the fuel consumed in boreal forest and tundra fires[26], below-ground fuel dryness from permafrost thaw may play a crucial role in shaping Arctic–boreal fire activity and emissions[13,27]. Furthermore, thaw-induced warming, aridity and water balance deficit (Extended Data Fig. 10) also dehydrate the above-ground live fine fuel, surface litter and below-ground organic material, lowering fuel moisture contents and increasing flammability[34,42,43].

The thaw-induced amplification of fire regimes may in turn alter northern terrestrial ecosystems and the affected regional-to-global climates. Wildfires further accelerate permafrost degradation by raising soil temperatures, deepening active layers and expanding taliks and thermokarst bogs[7,10]. Beyond direct combustion emissions, fire-induced degradation enhances soil respiration and sustains carbon release for years to decades[10], potentially shifting northern ecosystems from carbon sinks to sources and amplifying climate change[5]. Once initiated, these permafrost–fire–climate feedbacks threaten the stability and functioning of northern ecosystems (Fig. 4).

Implications and limitations

Our study uncovers a previously overlooked cascade through which the permafrost thaw amplifies Arctic–boreal summer fire regimes. We show that the permafrost thaw simultaneously intensifies fire weather, enhances vegetation growth and dries below-ground fuels, collectively increasing fire activity and emissions. These cascading effects create positive fire–climate feedbacks that threaten the stability of Arctic–boreal ecosystems and further accelerates climate change. While previous climate simulations have highlighted the potential climatic feedbacks from permafrost thaw and their potential impacts on wildfire activitiy[20,21], direct observational evidence has been limited. Our study

https://doi.org/10.1038/s41561-025-01894-y

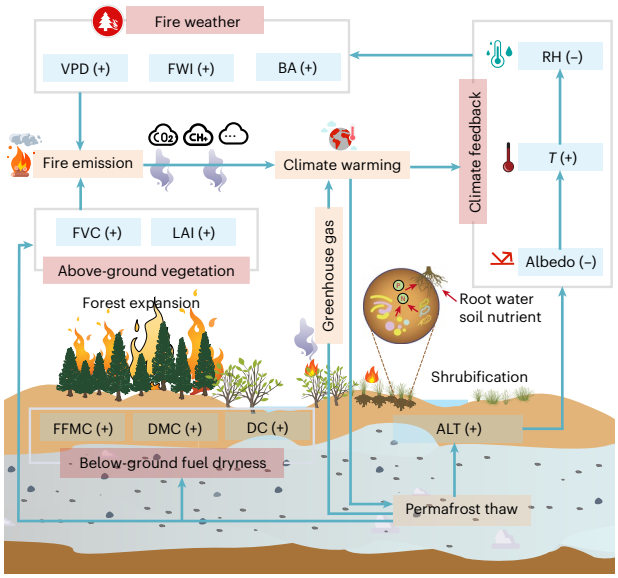

Fig. 4 | Conceptual framework of the permafrost–fire–climate feedback in northern high latitudes. This schematic summarizes the mechanistic pathways identified in this study. The permafrost thaw deepens the active layer (ALT), altering soil hydrology and nutrient availability, which promotes vegetation increases (higher FVC and LAI) and shifts in plant community composition, including forest expansion in boreal regions and shrubification in the tundra. These thaw-driven vegetation changes reduce surface albedo and increase surface air temperature, contributing to a warmer and drier atmosphere (higher *T* and VPD and lower RH). At the same time, thaw-induced soil drying enhances below-ground fuel dryness (increased FFMC, DMC and DC), intensifying fire weather conditions (higher FWI) and thereby increasing BA and fire emissions. The elevated fire emissions of CO_2, CH_4 and other trace gases, along with the biophysical warming effects of permafrost thaw, reinforce regional climate warming, which feeds back to further permafrost degradation. Together, these linked processes constitute a positive permafrost–fire–climate feedback loop. The plus and minus symbols denote increases and decreases, respectively.

provides such evidence by (1) identifying the key mechanisms linking thaw to fire regimes, (2) demonstrating the role of vegetation increases and below-ground fuel dryness in shaping Arctic–boreal wildfires and (3) quantifying the additional burned area and fire emissions attributable to permafrost thaw.

Identifying the climatic feedbacks from permafrost thaw is challenging owing to their complex interactions[7,20]. A key contribution of our study is the integration of the CCM model and SFT approach to address this bidirectional system. Uncovering cause–effect relationships is essential for revealing the mechanisms driving Earth system dynamics[44]. The SFT assumes that neighbouring pixels share the same background climate as the central pixel[29,45,46]. Moreover, this method only quantifies the local climatic impacts of permafrost thaw, ignoring large-scale feedbacks mediated by atmospheric circulation[45]. Despite these limitations, our findings are supported by regional climate model simulations showing that permafrost thaw amplifies summer fire severity, mainly by reducing relative humidity through a series of biophysical feedbacks[20]. Therefore, our results provide a valuable benchmark for evaluating the sensitivity of these interactions as simulated by land surface models.

It should be noted that our study provided only preliminary lower-bound estimates of the additional burned area and fire emissions induced by permafrost thaw. This is because non-linear models based on FWI represent a simplified depiction of fire spread and ignition[47], which can explain on average 53% of burned area variations, though exceeding 80% in some regions (Extended Data Fig. 8). The remaining variation is probably attributed to ignition sources, fuel availability and flammability that were not incorporated into our model. Process-based fire models explicitly incorporate the complex effects of climate, vegetation dynamics, fuel moisture, ignition sources and human activity on wildfires. However, to the best of our knowledge, current process-based fire models are rarely coupled with permafrost modules and thus cannot capture fire–permafrost interactions. By contrast, our regression-based framework provides a more data-driven, simplified and efficient way to preliminarily quantify the impacts of permafrost thaw on fire regimes. Future efforts should focus on advancing process-based models by coupling climate, land surface, permafrost and fire components to improve the understanding and quantification of permafrost–fire–climate feedbacks. In parallel, data-driven fire models should more comprehensively consider the effects of climate, vegetation, ignition and human activity. Such improvements would enable cross-validation with process-based models and strengthen the estimates of fire regime changes induced by permafrost thaw.

Our study probably underestimates the carbon–climate feedback within the broader permafrost–fire–climate feedback loop, because it provides only preliminary lower-bound estimates of carbon emissions directly from fire due to permafrost thaw. This feedback could be substantially amplified when further considering the prolonged carbon release following fire-induced permafrost degradation, a process that could continue to impact the climate for decades[3,10]. Accurate estimates of carbon flux within this positive feedback loop are crucial for understanding the carbon budget and projecting future climate change in Arctic–boreal ecosystems. However, these estimates remain challenging owing to the complex processes involved, including direct fire emissions[48], carbon release from permafrost degradation[49] and carbon sequestration by enhanced vegetation growth[50]. Our results highlight the need to incorporate thaw-driven fire and vegetation feedbacks into climate models and underscore the urgent importance of developing strategies to mitigate and adapt to accelerating climate change.

Datasets of ALT

The deepening ALT was used to indicate permafrost thaw across the northern permafrost zone (>45° N). We excluded the Tibetan Plateau owing to the rarity of wildfires in this region. We obtained ALT ground measurements from 86 sites within the CALM network[51] (Supplementary Fig. 1). The sites were selected on the basis of the following criteria: (1) latitudes >45° N and (2) providing at least 10 years of consecutive ALT observations from 1997 to 2018.

We also applied a long-term ESA hemispheric ALT product (version 3.0) with 1 km resolution for 1997–2018. The ALT is derived from a thermal model driven and constrained by satellite observations[52]. We resampled ALT data to a resolution of 0.05° using the nearest-neighbour method. We selected a 0.05° aggregation scale for two main reasons: (1) in the absence of higher-resolution data, 0.05° is widely used in SFT analyses to estimate sensitivity, as it helps ensure the assumption of a similar climate background between the central pixel and its adjacent pixels[29,53,54], and (2) it provides a balance between reducing downscaling errors from other datasets (for example, ERA5-Land at 0.1° and the fire weather dataset at 0.25°) and maintaining computational efficiency. Long-term trends in ALT were determined using the Mann–Kendall test and the Theil–Sen estimator. We also used the latest version of the ESA ALT product (version 4.0) to extend the time series to 1997–2021.

FWI and burned area

We used summer (June–August) FWI and burned area from 1997 to 2018 to assess fire weather conditions and fire activity. The FWI was obtained from a high-resolution reanalysis dataset of global fire weather produced on the basis of the Canadian FWI System (CFWIS)[55]. The CFWIS considers surface temperature, relative humidity, 24-h accumulated rainfall and wind speed to calculate three moisture codes for three fuel layers, which are then used to estimate the potential rate of spread, available fuel and fire intensity[56,57]. The components of CFWIS are widely used in both operational applications and scientific research at regional

and global scales[58–60]. This dataset applied two methods for setting the start-up value of the DC at the start of the fire season when calculating FWI. One method sets the DC to its default start-up value at the beginning of each fire season, while the other uses the overwintered DC value, calculated on the basis of the DC value of the last day of the previous fire season and a fraction of accumulated overwinter precipitation. The latter method considers interseasonal drought effects[55]. In this study, we used the FWI data that incorporate the overwintering procedure, as they better reflect drier fuel moisture conditions in regions with low overwinter precipitation, such as western North America and the Siberian boreal forest, resulting in more accurate FWI estimates[55].

The burned area in the northern permafrost zone was identified using the most recent GFED5, which included small fires[61]. This database provides monthly total burned area with resolutions of 0.25° for 2001–2018 and 1° for 1997–2000. We thus aggregated summer (June–August) FWI and total burned area within a 1° grid cell. In GFED5, although 500-m MODIS burned area products serve as the main sources of the time series, it also combines information from finer-resolution satellite imagery (Landsat and Sentinel-2) to reduce omission and commission errors. Compared with other datasets, the GFED5 estimates of global burned area are 93% higher than 500-m MCD64A1, 61% higher than GFED4s and in closer agreement with products from higher-resolution satellite sensors[61]. Therefore, GFED5 helps mitigate omission errors from small fires in high-latitude regions.

Vegetation growth and below-ground fuel dryness

FVC and LAI were used to represent above-ground vegetation biomass, coverage and connectivity, which determine the availability and continuity of live fuels. FVC was derived from MODIS and AVHRR data of the long-term Global Land Surface Satellite (GLASS) V40 product. This product provides 8-day and 0.05° FVC observations[62]. LAI was from the most recent version of the Global Inventory Modelling and Mapping Studies LAI product (GIMMS LAI4g), which provides spatiotemporally consistent half-monthly global LAI observations with a resolution of 1/12° (ref. 63). LAI and FVC were resampled to a resolution of 0.05° using a bilinear interpolation method and averaged to the summers during 1997–2018.

For below-ground fuel dryness, we used three indices over 1997–2018 from a high-resolution reanalysis dataset of global fire weather with a spatial resolution of 0.25°: FFMC, DMC and DC. These indices were calculated on the basis of the CFWIS and considering an overwintering procedure[55]. Specifically, FFMC serves as an indicator of the moisture content of the top litter layer less than 1–2 cm deep, including litter and other cured fine fuels (needles, mosses and twigs less than 1 cm in diameter). The DMC represents the moisture content in loosely compacted organic layers at moderate depths of 5–10 cm. The DC characterizes the moisture content in deep compact organic layers at approximately 10–20 cm depth[56,64]. Higher values of these three indices indicate higher moisture deficiency and flammability. Note that although FFMC is more closely associated with surface fine fuels[56,64], it was uniformly classified as a below-ground fuel dryness variable, together with DMC and DC. This classification helps distinguish them from other types of variable. The daily variables were resampled to a resolution of 0.05° using a bilinear interpolation method and averaged to the summers during 1997–2018.

Climatic data

We collected monthly climatic data, including air temperature (T) and dewpoint temperature (T_d) at a height of 2 m, surface albedo, relative humidity (RH), VPD, flux of surface sensible heat (H) and surface soil moisture content (SM) with a resolution of 0.1° for 1997–2018 from the ERA5-Land reanalysis dataset[65]. VPD and RH were calculated using monthly T and T_d on the basis of ref. 66. The monthly CWD at a resolution of 4 km was obtained from the TerraClimate dataset[67]. VPD and RH, directly measuring atmospheric aridity, play crucial roles in determining fire weather conditions[68] and the dynamics of fire[69]. CWD, defined as the difference between potential and actual evapotranspiration, serves as a proxy for the water balance deficit between the land surface and the atmosphere, thus indicating plant water stress and fuel flammability[17]. All climatic data were resampled to a resolution of 0.05° using a bilinear interpolation method and were averaged from June to August to represent summer climatic conditions.

Auxiliary data

The biophysical feedbacks to local climate induced by deepening ALT can be confounded by vegetation dynamics[70], changes to land use and cover[32] and topography[29]. We used FVC from the GLASS V40 product and LAI from the GIMMS LAI4g product to represent vegetation dynamics. We used the long-term 300-m dataset (v2.0.8) of global plant functional types (PFTs) to determine the changes in land use and cover. This product provides 14 layers, each of which describe the percent coverage of a PFT[71]. We considered three categories of vegetation underlain by permafrost: trees (broadleaved evergreen trees, broadleaved deciduous trees, needleleaved evergreen trees and needleleaved deciduous trees), shrubs (broadleaved evergreen shrubs, broadleaved deciduous shrubs, needleleaved evergreen shrubs and needleleaved deciduous shrubs) and grasses (managed and natural grasses). Bare areas, areas of permanent snow and ice, water bodies and built-up areas were excluded because we considered that no fire can occur in them. We aggregated this product from the native resolution into 0.05° grid cells by identifying the main types of vegetation (trees, shrubs and grasses) and calculating the corresponding maximum percent coverage for each year. We also used the GMTED2010 digital elevation model to eliminate the potential interference of topographic variation, because topography plays an important role in controlling the influence of permafrost thaw on land surface processes[14].

Causal discovery by CCM model

Uncovering cause–effect relationships is essential for understanding the underlying mechanistic interactions within the Earth system[44,72]. CCM[31], a causal inference model, has been widely used in socioeconomics[73], environmental pollution[28] and ecological research[72]. We applied this model to discover the causality of feedbacks initiated by permafrost thaw. While CCM can reliably discover both unidirectional and bidirectional causal associations between variables over time[28,31,72], our focus was on the unidirectional causal effects of permafrost thaw (increased ALT) on summer meteorological conditions favourable to fire (for example, VPD and CWD), vegetation growth (for example, FVC and LAI) and below-ground fuel dryness (for example, FFMC, DMC and DC). The CCM model identifies the causality of 'x causes y' based on non-linear state space reconstruction (Extended Data Fig. 1). The model first constructs shadow manifolds (the state space constructed from lagged coordinates of the time series of a variable) for variable x and y according to

$$M_{x,t} = [x_t, x_{t-\tau}, x_{t-2\tau}, \cdots, x_{t-(E-1)\tau}] \quad (1)$$

$$M_{y,t} = [y_t, y_{t-\tau}, y_{t-2\tau}, \cdots, y_{t-(E-1)\tau}] \quad (2)$$

where $M_{x,t}$ and $M_{y,t}$ are the shadow manifolds of x and y at time t, respectively. τ is the time lag, E is the number of dimensions and x_t and y_t are the observed values of x and y at time t, respectively. Then, the model uses the manifold of y (M_y) to predict the state of x ($M_x|M_y$). The correlation coefficient between the predicted ($M_x|M_y$) and observed states (M_x) of variable x is next calculated, assessed by the predictive skill (ρ). If ρ converges as the increase of time series length (L), we can infer that 'x causes y', that is, x causally affects y (refs. 31,72). We assessed this convergence by calculating the Spearman's rank correlation between ρ and L, identifying causality only when the correlation was significantly positive[33].

We used the rEDM R package[31] to perform CCM causal discovery, utilizing site-level ALT ground measurements from the CALM

network and the ESA hemispheric ALT product. The time to prediction was set to zero to detect the contemporaneous causal links between variables. We focused on the contemporaneous causality because the available hemispheric ALT data are yearly, which prevents us from examining the seasonal lagged causal effect of deepening ALT on summer climate and landscape. E and τ were set to 3 and 1, respectively, meaning that shadow manifolds were constructed in a three-dimensional state space using the original and two time-lagged series (equations (1) and (2)).

Long-term climate trends may influence the CCM in identifying a causal relationship. For example, rising temperature can simultaneously drive both deepening ALT and increasing VPD. Therefore, we used the year-to-year variations of these variables (defined as the difference between two consecutive years) as the input time series to eliminate the influence of long-term climate trends when running the CCM model. In addition, to reinforce the robustness of our CCM-based causal analysis, we applied multivariate CCM to assess the causal relationship between ALT and VPD while excluding the confounding effect of rising temperature on VPD and compared the results with those from the original CCM. As shown in Supplementary Fig. 3, the causal effect of ALT on VPD was strengthened after controlling for rising temperature.

CCM determines causality by testing whether predictive skill converges as the time series length increases. Therefore, limited observations and data noise can constrain convergence and reduce the reliability of causal inference. The relatively short record of hemispheric ALT (22 years) may affect CCM performance. Nevertheless, our results consistently reveal causal links between permafrost thaw and fire-prone meteorological conditions, vegetation growth and below-ground fuel dryness across large areas of the permafrost zone. In addition, CCM cannot distinguish whether two variables are causally related directly or indirectly. To address this, we further applied an SEM to disentangle direct and indirect feedback processes (Methods and Extended Data Fig. 10).

Estimation of the feedbacks from permafrost thaw based on the SFT approach

We used the SFT approach[29] to quantify the sensitivities of summer meteorological conditions (for example, VPD, CWD, albedo, T and RH), vegetation growth (for example, FVC and LAI) and below-ground fuel dryness (for example, FFMC, DMC and DC) to increased ALT. It assumes that the background climate is consistent between the central and adjacent pixels; therefore, differences in these variables between the central and adjacent pixels under specific constraints can be primarily attributed to changes induced by the permafrost thaw. This approach, widely used to detect the climatic feedbacks of vegetation dynamics and land-cover change[32,53], was adapted to quantify the biophysical and biological feedbacks induced by permafrost thaw in our study. Long-term trends and fluctuations of the climate system influence both permafrost and climate variations, resulting in complex two-way interactions between permafrost and climate. In such cases, the purely temporal regression strategy may conflate these bidirectional effects and overestimate the regional signals of 'permafrost feedback to climate'[29]. By contrast, the SFT approach is better suited to disentangling such bidirectional dynamics, allowing us to separate the unidirectional feedbacks of permafrost thaw on local climate and landscape, as the sensitivity is regressed from simultaneous ALT and climatic observations from spatial samples that share the same background climate[29].

Our method was similar to that presented in ref. 29, as demonstrated in Extended Data Fig. 2, to eliminate the influence of vegetation dynamics, changes to land use and cover and topography. For each year and each 0.05° pixel, we selected neighbouring pixels within a spatial moving window with 9 pixels × 9 pixels on the basis of the following criteria: (1) the types of permafrost and main land cover (that is, trees, shrubs or grasses) of the surrounding pixels should match those of the central pixel, (2) the difference in LAI between the selected and central pixels should be <0.1 $m^2 m^{-2}$, (3) changes to vegetation coverage should be <10%, (4) changes to the percent coverage of the main land-cover type should be <10% and (5) the difference in the digital elevation model should be <100 m. We also constrained a minimum difference in ALT exceeding 1 cm between the selected and central pixels to reduce uncertainty from the noise of the input data. The annual sensitivity of each factor to ALT was then estimated for the central pixel by regressing ALT against the factor values using all adjacent pixels satisfying the criteria, along with the central pixel itself. To enhance robustness, we used Theil–Sen regression, which is insensitive to statistical outliers and required a minimum of four valid samples for each regression. Finally, the 22-year average sensitivity was calculated to represent the overall sensitivity to changes in ALT from 1997 to 2018. It should be noted that vegetation dynamics were not used as constraints when selecting adjacent pixels for calculating the sensitivity of FVC and LAI to ALT. Moreover, the effects of CO_2 fertilization on vegetation growth were excluded from the SFT approach, as changes in CO_2 concentration can be considered spatially uniform within the spatial window.

In addition, we evaluated the robustness of the sensitivity estimates from the SFT approach through the following aspects: (1) we used the latest version of ESA hemispheric ALT data (version 4.0) to perform the same SFT analysis from 1997 to 2021 (Supplementary Fig. 5). (2) We incorporated an additional constraint to ensure a similar climate background between the central pixel and its adjacent pixels (Supplementary Fig. 10). Specifically, differences in air temperature and precipitation between the central pixel and selected adjacent pixels were required to be less than 10% (refs. 45,46). (3) To validate the robustness of estimates from different sizes of the spatial moving window, we tested 7 pixels × 7 pixels (Supplementary Fig. 11) and 11 pixels × 11 pixels (Supplementary Fig. 12). (4) To validate the robustness of estimates from different spatial resolution, we tested the resolution of 0.1° (Supplementary Fig. 13) and 0.25° (Supplementary Fig. 14). (5) To validate the robustness of estimates from different resample methods, we used the bilinear interpolation method (Supplementary Fig. 15) and the area-weighted average method (Supplementary Fig. 16) to upscale the ESA hemispheric ALT from 1 km to 0.05°. Overall, all above robustness analyses consistently supported our main findings, indicating that a deepening ALT could amplify meteorological drought, enhance vegetation growth and intensify below-ground fuel dryness.

Feedbacks from seasonal dynamics of permafrost thaw

In addition to the annual record of ALT, the active layer above permafrost undergoes seasonal thawing and freezing. Therefore, shifts in key phases of the annual freeze–thaw cycle can serve as indicators of permafrost thawing. For example, the start of thaw (SOT) has advanced across the northern permafrost zone over the past four decades[74]. To capture this, we used the Freeze–Thaw Earth System Data Record (FT-ESDR), which provides daily land surface freeze–thaw status derived from satellite microwave brightness temperature observations. The daily land surface status includes frozen, thawed, transitional and inverse transitional[75]. We used FT-ESDR to estimate annual SOT from 1997 to 2018[74]. Then, we used the CCM model to qualitatively assess causal relationships between SOT and multiple variables and the SFT approach to quantificationally estimate the sensitivities. The CCM results supported causal relationships between SOT and VPD, FVC, LAI, FFMC, DMC and DC across large areas of northern permafrost zone (Supplementary Fig. 17). The sensitivity estimates further supported our main findings, indicating that an earlier SOT could decrease albedo and RH, while increasing T, VPD, FVC, LAI, FFMC, DMC and DC (Supplementary Fig. 18). Given that SOT typically occurs in spring, these analyses provide an alternative way to explore the seasonal lagged effects of permafrost thaw on summer climate and landscape.

XGBoost-based fire weather modelling

We estimated the feedback between permafrost thaw and fire weather conditions by applying XGBoost to model the summer FWI variations (ΔFWI) as a function of variations in summer T (ΔT), VPD (ΔVPD) and RH (ΔRH)

$$\Delta\mathrm{FWI} = \mathrm{XGBoost}(\Delta T, \Delta\mathrm{RH}, \Delta\mathrm{VPD}) \quad (3)$$

where Δ operator indicates year-to-year variation calculated as the difference between two consecutive years. The relative contributions of selected predictors to FWI variations differ across regions[68]; therefore, we developed four region-specific XGBoost FWI models for the GFED regions within the northern permafrost zone: North America (including boreal North America and temperate North America), Europe, boreal Asia and Central Asia (Supplementary Fig. 6). The models produced sample sizes of 43,254, 13,187, 57,350 and 17,092 for North America, Europe, boreal Asia and Central Asia, respectively (Extended Data Fig. 6). The dataset for each model was randomly split into training and testing sets at a 4:1 ratio, and this process was repeated 10,000 times to quantify the uncertainties in ΔFWI estimations.

We selected T, RH and VPD as predictors for two main reasons: first, T and RH are key inputs in the CFWIS for calculating FWI; second, rising temperatures and declining atmospheric humidity have been the primary drivers of global trends in extreme FWI over the past four decades[68]. In addition, the XGBoost-based FWI models we developed performed strongly in predicting FWI variations across GFED regions, explaining 82–95% of the FWI variability (Extended Data Fig. 6).

Variations of FWI and burned area induced by changes in ALT

We calculated changes in summer FWI induced by deepening ALT from 1997 to 2018. First, the change in ALT over the 22-year period (denoted as ΔALT) was calculated by multiplying the annual ALT trend by the number of years. Second, both the overall sensitivities derived from the SFT approach and the ΔALT map were aggregated to a 1° resolution by averaging values within each larger grid cell. Third, we quantified changes in individual climatic variables driven by deepening ALT (namely ΔT, ΔVPD and ΔRH) by multiplying ΔALT by the corresponding 22-year overall sensitivities. Finally, we input ΔT, ΔVPD and ΔRH into the XGBoost-based FWI models to estimate ΔFWI across the northern permafrost zone. The ΔFWI and its uncertainty were calculated as the mean and standard deviation from 10,000 bootstrapped simulations, respectively.

We also provided a preliminary estimate of changes in burned area associated with permafrost thaw. At the grid-cell level (1°), we observed an approximately cubic relationship between changes in summer FWI and total burned area (Extended Data Fig. 8b). Accordingly, we applied a cubic function to model the non-linear relationship between them (equation (4))

$$\Delta\mathrm{BA} = a \times \Delta\mathrm{FWI}^3 + b \times \Delta\mathrm{FWI}^2 + c \times \Delta\mathrm{FWI} + d \quad (4)$$

where Δ operator represents year-to-year variation calculated by the difference between two consecutive years. The fitted parameters (a, b, c and d) and their corresponding standard deviations were optimized by using the Levenberg–Marquardt algorithm, a non-linear least squares method. For each grid cell, we used a spatial moving window with 3 × 3 grid cells to increase the sample size. To enhance model stability, the model was trained using mean ΔBA values within 20 equally spaced ΔFWI bins.

Moreover, we used the initial spread index (ISI) and the annual extreme values of FWI and ISI (denoted as FWI_{95} and ISI_{95}) to construct alternative non-linear burned area models. The ISI represents the potential rate of fire spread and is closely associated with the expansion of burned areas[68]. ISI was also derived from the global fire weather data set that considers an overwintering procedure. FWI_{95} and ISI_{95} refer to the 95th percentile of annual values of FWI and ISI, respectively. They can characterize the extreme fire weather conditions that are closely linked to daily fire spread and burned area growth[76]. Given the strong positive correlation between FWI and total burned area in northern ecosystems[47], we also assessed a linear model for comparison with the cubic model. Model performance was evaluated using the determination coefficient (R^2) and mean absolute error. The cubic model relating summer ΔFWI and ΔBA provided the best fit, yielding the highest R^2 values of 0.53 (Extended Data Fig. 8). Accordingly, we used this cubic model to translate ΔFWI into additional burned areas associated with permafrost thaw.

The uncertainty of estimated changes in burned area was quantified using Monte Carlo simulations, accounting for uncertainty propagation from ΔFWI. For each grid cell, ΔBA was estimated 10,000 times using different random combinations extracted from the normal distributions of ΔFWI and the four fitted parameters in cubic function. The normal distribution was defined by their means and standard deviations. The final reported estimates are the mean and standard deviation of the ΔBA values obtained in the 10,000 iterations.

Fire emissions

Fire releases large amounts of carbon into the atmosphere by combusting plant and soil organic material, thereby influencing regional to global climates. We therefore estimated fire emissions associated with the deepening ALT (noted as ΔEmission) using the GFED method[48]. This method applies a bottom-up fire emission model that considers burned area, total fuel consumption per unit burned area, fraction of contribution for different types of fire and emission factors (equation (5)):

$$\Delta E_S = \sum_{\mathrm{source}} \Delta\mathrm{BA} \times \mathrm{FC} \times \mathrm{contr}_{\mathrm{source}} \times \mathrm{EF}_{S_{\mathrm{source}}} \quad (5)$$

where ΔE is the fire emissions, S is the gas species (CO_2 and CH_4 in this study), source is the type of fire, including boreal forest, peat, savanna (SAVA) and temperate forest in the northern permafrost zone, ΔBA is the change to burned area induced by the deepening ALT (Fig. 3f), FC is the total fuel consumption per unit burned area (kg m^{-2} burned), contr is the fractional contribution for the type of fire and EF is the emission factor for different types of gas species and fire (gram species per kilogram of fuel burned). SAVA fire types include SAVA, grassland and shrubland fires in GFED4.1s[48]; therefore, we also considered SAVA fires in the northern permafrost zone.

Fuel consumption, the fractional contribution of different types of fire and the emission factors were determined from the GFED4.1s dataset for 1997–2018[48]. Specifically, we obtained monthly data for grid-cell burned area (m^2) and emissions of dry matter (kg) at a resolution of 0.25° from GFED4.1s. These data were summed into summer totals within 1° grid cells. Fuel consumption for each year was calculated as the ratio of emissions from dry matter to the total burned area. The 22-year annual mean and standard deviation were used as the reference values of FC (kg m^{-2} burned) and the corresponding variability (Supplementary Fig. 8a,b). We note that fuel consumption indicates the dry matter, rather than the carbon. The monthly fractional contribution of each type of fire from GFED4.1s was then averaged for summer and within 1° × 1° grid cells, weighted by emissions from dry matter. Similarly, the 22-year annual mean and standard deviation were used as reference values of contr and the corresponding variability (Supplementary Fig. 9). We used GFED4.1s emission factors[48] to convert fuel consumption to CO_2 and CH_4 emissions. The emission factors and their uncertainties for CO_2 and CH_4 across the four types of fire were determined on the basis of the compilation in ref. 77 (Supplementary Table 2). By contrast, we specifically used emission factors collected in boreal peat for the peat fires[77,78].

We also used the most recent high-resolution data for fuel consumption at resolution of 500 m, which estimated higher fuel consumption in boreal regions compared with GFED4.1s[26] (Supplementary Fig. 8). We used the monthly 0.25-degree aggregated carbon emissions and burned area from this dataset for 2002–2022 to calculate fuel consumption. The total carbon emissions from biomass burning include contributions from both above- and below-ground sources. We applied a factor of 2 to convert the carbon emissions to units of dry matter[17]. Dry matter consumption and burned area were then summed into summer totals within 1° × 1° grid cells. Annual fuel consumption was calculated as the ratio of dry matter consumption to the total burned area. The 22-year annual mean and standard deviation served as the reference values for *FC* (kg m^{-2} burned) and its variability, respectively (Supplementary Fig. 8c,d).

The uncertainty of our estimates of fire emissions was assessed using Monte Carlo simulations, which accounted for the propagation of variabilities in FC (Supplementary Fig. 8), contr (Supplementary Fig. 9) and EF (Supplementary Table 2), as well as the uncertainty of ΔBA. CO_2 and CH_4 emissions were estimated 10,000 times for each grid cell using randomly sampled combinations from normal distributions of ΔBA, FC, contr and EF defined by their means and standard deviations. The emission factors for peat fires, however, were treated as uniformly distributed, bounded by absolute values within the range of EF[77,78] (Supplementary Table 2). The final estimates of the CO_2 and CH_4 emissions were derived from the means and standard deviations of the values obtained in the 10,000 iterations.

However, it should be noted that fire emissions derived from both datasets are probably underestimated. Although GFED4.1s includes more burned area by accounting for small fires that are undetected by the MODIS burned area algorithm, its small fire layer remains subject to considerable uncertainty[48]. In addition, lower estimates of fuel consumption in GFED4.1s contribute to underestimations in boreal regions[26]. By contrast, the 500-m fuel consumption dataset accounts for higher fuel consumption in boreal areas but underestimates fire emissions owing to the omission of small fires[26]. Therefore, high-resolution satellite imagery—such as 30-m Landsat or 20-m Sentinel-2—is essential for generating finer burned area products and improving fire emission estimates[26].

SEM

We used the SEM to elucidate the underlying mechanisms and causal connections among feedback processes triggered by permafrost thaw, including the feedback effects on meteorological conditions favorable to fire (pathway A and B), vegetation growth (pathway B) and below-ground fuel dryness (pathway C) (Extended Data Fig. 10). Surface soil moisture plays a crucial role in regulating exchanges of energy and water between the terrestrial surface and the atmosphere[79]. We thus considered surface soil moisture, which can modify the flux of surface sensible heat, as a mediator between deepening ALT and increased air temperature in pathway A. We also accounted for the effect of vegetation dynamics on local climate by regulating surface albedo[29,53] in pathway B. Pathway B also included the impact of permafrost thaw on northern vegetation growth[14], potentially enhancing above-ground fuel availability and connectivity. The SOC accounts for a large proportion of the fuel consumed in boreal forest and tundra fires[26]; therefore, we designed pathway C to describe the impact of permafrost thaw on below-ground fuel dryness, mainly driven by changes in surface soil moisture.

We used the lavaan R package to construct the SEM, combining maximum likelihood estimation with bootstrapping to derive standardized path coefficients at the grid-cell level. Bootstrapping provides robust estimates of path coefficients, standard errors and *P* values without relying on data distributional assumptions. To ensure model stability, the SEM was performed using normalized year-to-year variations of all variables, calculated by dividing the difference between two consecutive years by the 22-year standard deviations. Path coefficients describe the strength and sign of the relationships between connected variables.

Online content

Any methods, additional references, Nature Portfolio reporting summaries, source data, extended data, supplementary information, acknowledgements, peer review information; details of author contributions and competing interests; and statements of data and code availability are available at https://doi.org/10.1038/s41561-025-01894-y.

References

1. Koven, C. D. et al. Permafrost carbon-climate feedbacks accelerate global warming. *Proc. Natl Acad. Sci. USA* **108**, 14769–14774 (2011).
2. Hugelius, G. et al. Estimated stocks of circumpolar permafrost carbon with quantified uncertainty ranges and identified data gaps. *Biogeosciences* **11**, 6573–6593 (2014).
3. Miner, K. R. et al. Permafrost carbon emissions in a changing Arctic. *Nat. Rev. Earth Environ.* **3**, 55–67 (2022).
4. Schuur, E. A. G. et al. Climate change and the permafrost carbon feedback. *Nature* **520**, 171–179 (2015).
5. Turetsky, M. R. et al. Carbon release through abrupt permafrost thaw. *Nat. Geosci.* **13**, 138–143 (2020).
6. Hjort, J. et al. Impacts of permafrost degradation on infrastructure. *Nat. Rev. Earth Environ.* **3**, 24–38 (2022).
7. Smith, S. L., O'Neill, H. B., Isaksen, K., Noetzli, J. & Romanovsky, V. E. The changing thermal state of permafrost. *Nat. Rev. Earth Environ.* **3**, 10–23 (2022).
8. Peng, X. et al. Active layer thickness and permafrost area projections for the 21st century. *Earth Future* **11**, e2023EF003573 (2023).
9. Dobiński, W. Permafrost active layer. *Earth Sci. Rev.* **208**, 103301 (2020).
10. Gibson, C. M. et al. Wildfire as a major driver of recent permafrost thaw in boreal peatlands. *Nat. Commun.* **9**, 3041 (2018).
11. Jones, B. M. et al. Recent Arctic tundra fire initiates widespread thermokarst development. *Sci. Rep.* **5**, 15865 (2015).
12. Finney, D. L. Lightning threatens permafrost. *Nat. Clim. Change* **11**, 379–380 (2021).
13. Zhu, X., Xu, X. & Jia, G. Recent massive expansion of wildfire and its impact on active layer over pan-Arctic permafrost. *Environ. Res. Lett.* **18**, 084010 (2023).
14. Heijmans, M. M. P. D. et al. Tundra vegetation change and impacts on permafrost. *Nat. Rev. Earth Environ.* **3**, 68–84 (2022).
15. Webb, E. E. et al. Permafrost thaw drives surface water decline across lake-rich regions of the Arctic. *Nat. Clim. Change* **12**, 841–846 (2022).
16. Webb, E. E., Loranty, M. M. & Lichstein, J. W. Surface water, vegetation, and fire as drivers of the terrestrial Arctic-boreal albedo feedback. *Environ. Res. Lett.* **16**, 084046 (2021).
17. Descals, A. et al. Unprecedented fire activity above the Arctic Circle linked to rising temperatures. *Science* **378**, 532–537 (2022).
18. Lai, G. & Zhang, Y. Increased atmospheric aridity and reduced precipitation drive the 2023 extreme wildfire season in Canada. *Geophys. Res. Lett.* **52**, e2024GL114492 (2025).
19. Pausas, J. G. & Keeley, J. E. Wildfires and global change. *Front. Ecol. Environ.* **19**, 387–395 (2021).
20. Teufel, B. & Sushama, L. Abrupt changes across the Arctic permafrost region endanger northern development. *Nat. Clim. Change* **9**, 858–862 (2019).
21. Kim, J.-E. et al. Interannual fires as a source for subarctic summer decadal climate variability mediated by permafrost thawing. *npj Clim. Atmos. Sci.* **6**, 84 (2023).

22. Keuper, F. et al. A frozen feast: thawing permafrost increases plant-available nitrogen in subarctic peatlands. *Glob. Change Biol.* **18**, 1998–2007 (2012).
23. Chen, Y. et al. Future increases in Arctic lightning and fire risk for permafrost carbon. *Nat. Clim. Change* **11**, 404–410 (2021).
24. Mekonnen, Z. A. et al. Arctic tundra shrubification: a review of mechanisms and impacts on ecosystem carbon balance. *Environ. Res. Lett.* **16**, 053001 (2021).
25. Tao, F. et al. Microbial carbon use efficiency promotes global soil carbon storage. *Nature* **618**, 981–985 (2023).
26. van Wees, D. et al. Global biomass burning fuel consumption and emissions at 500 m spatial resolution based on the Global Fire Emissions Database (GFED). *Geosci. Model Dev.* **15**, 8411–8437 (2022).
27. Zhu, X., Jia, G. & Xu, X. Accelerated rise in wildfire carbon emissions from Arctic continuous permafrost. *Sci. Bull.* **69**, 2430–2438 (2024).
28. Gao, B. et al. Causal inference from cross-sectional earth system data with geographical convergent cross mapping. *Nat. Commun.* **14**, 5875 (2023).
29. Li, Y. et al. Biophysical impacts of earth greening can substantially mitigate regional land surface temperature warming. *Nat. Commun.* **14**, 121 (2023).
30. Li, Y., Zeng, Z., Huang, L., Lian, X. & Piao, S. Comment on 'Satellites reveal contrasting responses of regional climate to the widespread greening of Earth'. *Science* **360**, eaap7950 (2018).
31. Sugihara, G. et al. Detecting causality in complex ecosystems. *Science* **338**, 496–500 (2012).
32. Liu, X. et al. Local temperature responses to actual land cover changes present significant latitudinal variability and asymmetry. *Sci. Bull.* **68**, 2849–2861 (2023).
33. Shen, M. et al. Can changes in autumn phenology facilitate earlier green-up date of northern vegetation?. *Agr. Meteorol.* **291**, 108077 (2020).
34. Littell, J. S. Drought and fire in the western USA: is climate attribution enough?. *Curr. Clim. Change Rep.* **4**, 396–406 (2018).
35. Bonan, G. B. Forests and climate change: forcings, feedbacks, and the climate benefits of forests. *Science* **320**, 1444–1449 (2008).
36. Schuur, E. A. G., Crummer, K. G., Vogel, J. G. & Mack, M. C. Plant species composition and productivity following permafrost thaw and thermokarst in Alaskan tundra. *Ecosystems* **10**, 280–292 (2007).
37. Iversen, C. M. et al. The unseen iceberg: plant roots in arctic tundra. *N. Phytol.* **205**, 34–58 (2014).
38. Peng, R. et al. Tree growth is connected with distribution and warming-induced degradation of permafrost in southern Siberia. *Glob. Change Biol.* **28**, 5243–5253 (2022).
39. Ogden, E. L., Cumming, S. G., Smith, S. L., Turetsky, M. R. & Baltzer, J. L. Permafrost thaw induces short-term increase in vegetation productivity in northwestern Canada. *Glob. Change Biol.* **29**, 5352–5366 (2023).
40. O'Donnell, J. A. et al. The effect of fire and permafrost interactions on soil carbon accumulation in an upland black spruce ecosystem of interior Alaska: implications for post-thaw carbon loss. *Glob. Change Biol.* **17**, 1461–1474 (2011).
41. Chave, J. et al. Frequent fires in ancient shrub tundra: implications of paleorecords for arctic environmental change. *PLoS ONE* **3**, e0001744 (2008).
42. Resco de Dios, V. et al. A semi-mechanistic model for predicting the moisture content of fine litter. *Agr. Meteorol.* **203**, 64–73 (2015).
43. Matthews, S. Dead fuel moisture research: 1991–2012. *Int. J. Wildland Fire* **23**, 78–92 (2014).
44. Runge, J., Gerhardus, A., Varando, G., Eyring, V. & Camps-Valls, G. Causal inference for time series. *Nat. Rev. Earth Environ.* **4**, 487–505 (2023).
45. Qin, Y., Wang, D., Ziegler, A. D., Fu, B. & Zeng, Z. Impact of Amazonian deforestation on precipitation reverses between seasons. *Nature* **639**, 102–108 (2025).
46. Smith, C., Baker, J. C. A. & Spracklen, D. V. Tropical deforestation causes large reductions in observed precipitation. *Nature* **615**, 270–275 (2023).
47. Jones, M. W. et al. Global and regional trends and drivers of fire under climate change. *Rev. Geophys.* **60**, e2020RG000726 (2022).
48. van der Werf, G. R. et al. Global fire emissions estimates during 1997–2016. *Earth Syst. Sci. Data* **9**, 697–720 (2017).
49. Koven, C. D. et al. A simplified, data-constrained approach to estimate the permafrost carbon–climate feedback. *Philos. Trans. R. Soc. A* **373**, 20140423 (2015).
50. Friedlingstein, P. et al. Global Carbon Budget 2023. *Earth Syst. Sci. Data* **15**, 5301–5369 (2023).
51. Nyland, K. E. et al. Long-term Circumpolar Active Layer Monitoring (CALM) program observations in Northern Alaskan tundra. *Polar Geogr.* **44**, 167–185 (2021).
52. Obu, J. et al. Northern Hemisphere permafrost map based on TTOP modelling for 2000–2016 at 1 km^2 scale. *Earth Sci. Rev.* **193**, 299–316 (2019).
53. Alkama, R. & Cescatti, A. Biophysical climate impacts of recent changes in global forest cover. *Science* **351**, 600–604 (2016).
54. Alkama, R. et al. Vegetation-based climate mitigation in a warmer and greener World. *Nat. Commun.* **13**, 606 (2022).
55. McElhinny, M., Beckers, J. F., Hanes, C., Flannigan, M. & Jain, P. A high-resolution reanalysis of global fire weather from 1979 to 2018—overwintering the drought code. *Earth Syst. Sci. Data* **12**, 1823–1833 (2020).
56. Van Wagner, C. E. *Development and Structure of the Canadian Forest Fire Weather Index System* (Canadian Forestry Service, 1987).
57. Wang, X. et al. cffdrs: an R package for the Canadian Forest Fire Danger Rating System. *Ecol. Process.* **6**, 5 (2017).
58. Luo, K., Wang, X., de Jong, M. & Flannigan, M. Drought triggers and sustains overnight fires in North America. *Nature* **627**, 321–327 (2024).
59. Wang, W. et al. Canadian forests are more conducive to high-severity fires in recent decades. *Science* **387**, 91–97 (2025).
60. Jolly, W. M. et al. Climate-induced variations in global wildfire danger from 1979 to 2013. *Nat. Commun.* **6**, 7537 (2015).
61. Chen, Y. et al. Multi-decadal trends and variability in burned area from the fifth version of the Global Fire Emissions Database (GFED5). *Earth Syst. Sci. Data* **15**, 5227–5259 (2023).
62. Jia, K. et al. Long-Term Global Land Surface Satellite (GLASS) fractional vegetation cover product derived from MODIS and AVHRR data. *IEEE J. Sel. Top. Appl. Earth Obs. Remote Sens.* **12**, 508–518 (2019).
63. Cao, S. et al. Spatiotemporally consistent global dataset of the GIMMS Leaf Area Index (GIMMS LAI4g) from 1982 to 2020. *Earth Syst. Sci. Data Discuss.* **15**, 4877–4899 (2023).
64. Vitolo, C. et al. ERA5-based global meteorological wildfire danger maps. *Sci. Data* **7**, 216 (2020).
65. Muñoz-Sabater, J. et al. ERA5-Land: a state-of-the-art global reanalysis dataset for land applications. *Earth Syst. Sci. Data* **13**, 4349–4383 (2021).
66. Yuan, W. et al. Increased atmospheric vapor pressure deficit reduces global vegetation growth. *Sci. Adv.* **5**, eaax1396 (2019).
67. Abatzoglou, J. T., Dobrowski, S. Z., Parks, S. A. & Hegewisch, K. C. TerraClimate, a high-resolution global dataset of monthly climate and climatic water balance from 1958-2015. *Sci. Data* **5**, 170191 (2018).
68. Jain, P., Castellanos-Acuna, D., Coogan, S. C. P., Abatzoglou, J. T. & Flannigan, M. D. Observed increases in extreme fire weather driven by atmospheric humidity and temperature. *Nat. Clim. Change* **12**, 63–70 (2022).

69. Grunig, M., Seidl, R. & Senf, C. Increasing aridity causes larger and more severe forest fires across Europe. *Glob. Change Biol.* **29**, 1648–1659 (2022).
70. Forzieri, G., Alkama, R., Miralles, D. G. & Cescatti, A. Satellites reveal contrasting responses of regional climate to the widespread greening of Earth. *Science* **356**, 1180–1184 (2017).
71. Harper, K. L. et al. A 29-year time series of annual 300 m resolution plant-functional-type maps for climate models. *Earth Syst. Sci. Data* **15**, 1465–1499 (2023).
72. Gao, B., Li, M., Wang, J. & Chen, Z. Temporally or spatially? Causation inference in Earth System Sciences. *Sci. Bull.* **67**, 232–235 (2022).
73. Huang, X., Silva, E. & Hassani, H. Causality between oil prices and tourist arrivals. *Stats* **1**, 134–154 (2018).
74. Li, J., Wu, C., Peñuelas, J., Ran, Y. & Zhang, Y. The start of frozen dates over northern permafrost regions with the changing climate. *Glob. Change Biol.* **29**, 4556–4568 (2023).
75. Kim, Y., Kimball, J. S., Glassy, J. & Du, J. An extended global Earth system data record on daily landscape freeze–thaw status determined from satellite passive microwave remote sensing. *Earth Syst. Sci. Data* **9**, 133–147 (2017).
76. Wang, X. et al. The potential and realized spread of wildfires across Canada. *Glob. Change Biol.* **20**, 2518–2530 (2014).
77. Akagi, S. K. et al. Emission factors for open and domestic biomass burning for use in atmospheric models. *Atmos. Chem. Phys.* **11**, 4039–4072 (2011).
78. Yokelson, R. J., Susott, R., Ward, D. E., Reardon, J. & Griffith, D. W. T. Emissions from smoldering combustion of biomass measured by open-path Fourier transform infrared spectroscopy. *J. Geophys. Res. Atmos.* **102**, 18865–18877 (1997).
79. Seneviratne, S. I. et al. Investigating soil moisture–climate interactions in a changing climate: a review. *Earth Sci. Rev.* **99**, 125–161 (2010).
80. Iturbide, M. et al. Implementation of FAIR principles in the IPCC: the WGI AR6 Atlas repository. *Sci. Data* **9**, 629 (2022).

[1]The Key Laboratory of Land Surface Pattern and Simulation, Institute of Geographical Sciences and Natural Resources Research, Chinese Academy of Sciences, Beijing, China. [2]International Institute for Earth System Sciences, Jiangsu Center for Collaborative Innovation in Geographical Information Resource Development and Application, Nanjing University, Nanjing, China. [3]Department of Earth and Environmental Sciences, Vanderbilt University, Nashville, TN, USA. [4]Department of Environmental Systems Science, Institute of Integrative Biology, ETH Zurich, Zurich, Switzerland. [5]CSIC, Global Ecology Unit, CREAF-CSIC-UAB, Barcelona, Spain. [6]CREAF, Barcelona, Spain. [7]Department of Earth Sciences, Faculty of Science, Vrije Universiteit Amsterdam, Amsterdam, the Netherlands. [8]Geography Research Unit, University of Oulu, Oulu, Finland. [9]Laboratoire des Sciences du Climat et de l´Environnement, CEA-CNRS-UVSQ, Université Paris Saclay, Gif-sur-Yvette, France. [10]Department of Earth System Science, University of California, Irvine, Irvine, CA, USA. [11]National Tibetan Plateau Data Center, State Key Laboratory of Tibetan Plateau Earth System, Environment and Resources, Institute of Tibetan Plateau Research, Chinese Academy of Sciences, Beijing, China. [12]These authors contributed equally: Jialing Li, Gengke Lai.
✉e-mail: wucy@igsnrr.ac.cn

Methods

To investigate the potential mechanisms by which permafrost thaw amplifies Arctic–boreal fire regimes, we used the CCM model to qualitatively assess causal relationships and an SFT approach to quantificationally estimate the effects of permafrost thaw on meteorological drought, vegetation growth and below-ground dryness. To preliminarily quantify changes in fire regimes induced by permafrost thaw, we further applied an XGBoost-based model to predict changes in fire weather conditions, a non-linear model to estimate changes in burned area and a bottom-up model to calculate associated changes in fire emissions. An uncertainty propagation was incorporated throughout the estimation of fire regimes change using Monte Carlo simulations (Extended Data Fig. 3).

Data availability

All data used in this study are freely and publicly accessible via the following links: CALM ALT field measurements, http://www.gwu.edu/~calm/; ESA permafrost ALT for the Northern Hemisphere, v3.0 and v 4.0, https://climate.esa.int/en/projects/permafrost/, GLASS FVC V40, https://github.com/IPCC-WG1/Atlas/tree/main; Circum-Arctic Map of Permafrost and Ground-Ice Conditions, https://nsidc.org/data/GGD318/versions/2; FT-ESDR, http://files.ntsg.umt.edu/data/FT_V5/, ERA5-Land, https://cds.climate.copernicus.eu/cdsapp#!/dataset/reanalysis-era5-land-monthly-means; TerraClimate, https://www.climatologylab.org/terraclimate.html; ESA PFTs dataset v2.0.8, https://maps.elie.ucl.ac.be/CCI/viewer/download.php; GMTED2010, https://www.usgs.gov/coastal-changes-and-impacts/gmted2010 and GFED4.1s, https://www.globalfiredata.org/. A high-resolution reanalysis of global fire weather data that considers an overwintering procedure is available via Zenodo at https://doi.org/10.5281/zenodo.3626193 (ref. 55). GFED5 is available via Zenodo at https://doi.org/10.5281/zenodo.7668424 (ref. 61). The 500-m fuel consumption dataset is available via Zenodo at https://doi.org/10.5281/zenodo.7229674 (ref. 26). GIMMS LAI4g is available via Zenodo at https://doi.org/10.5281/zenodo.8281930 (ref. 63). Data for Figs. 1–3 and Extended Data Figs. 4–10 are available via Zenodo at https://doi.org/10.5281/zenodo.17567754 (ref. 81).

Code availability

The code for the analysis is available via Zenodo at https://doi.org/10.5281/zenodo.17567754 (ref. 81).

References

81. Li, J., Lai, G. & Wu, C. Amplified Arctic–boreal fire regimes from permafrost thaw feedbacks. *Zenodo* https://doi.org/10.5281/zenodo.17567754 (2025).

Acknowledgements

This work was funded by the National Natural Science Foundation of China (grant no. 42125101) and the CAS Interdisciplinary Innovation Team (grant no. JCTD-2020-05). J.P. was funded by European Research Council Synergy grant no. ERC-SyG-2013-610028 IMBALANCE-P. J.P. was also financially supported by the Fundación Ramon Areces grant no. ELEMENTAL-CLIMATE, the Spanish Government grant no. PID2019-110521GB-I00 and the Catalan Government grant no. SGR 2017-1005. C.M.Z. was funded by the SNF Ambizione grant no. PZ00P3_193646. S.V. acknowledges funding from the European Research Council (ERC) through a Consolidator grant under the European Union's Horizon 2020 research and innovation programme (grant no. 101000987). This work was also supported by the Science and Technology Programme of Guangdong (grant no. 2024B1212070012).

Author contributions

C.W. designed the research. J.L., G.L. and C.W. wrote the first draft of the article. J.L. and G.L. analysed the data and performed the research. J.L. conducted the visualization. All authors assessed the research analyses and contributed to the writing of the article.

Competing interests

The authors declare no competing interests.

Additional information

Extended data is available for this paper at https://doi.org/10.1038/s41561-025-01894-y.

Supplementary information The online version contains supplementary material available at https://doi.org/10.1038/s41561-025-01894-y.

Correspondence and requests for materials should be addressed to Chaoyang Wu.

Peer review information *Nature Geoscience* thanks Sumanta Chatterjee and the other, anonymous, reviewer(s) for their contribution to the peer review of this work. Primary handling editor: Xujia Jiang and Carolina Ortiz Guerrero, in collaboration with the *Nature Geoscience* team.

https://doi.org/10.1038/s41561-025-01894-y

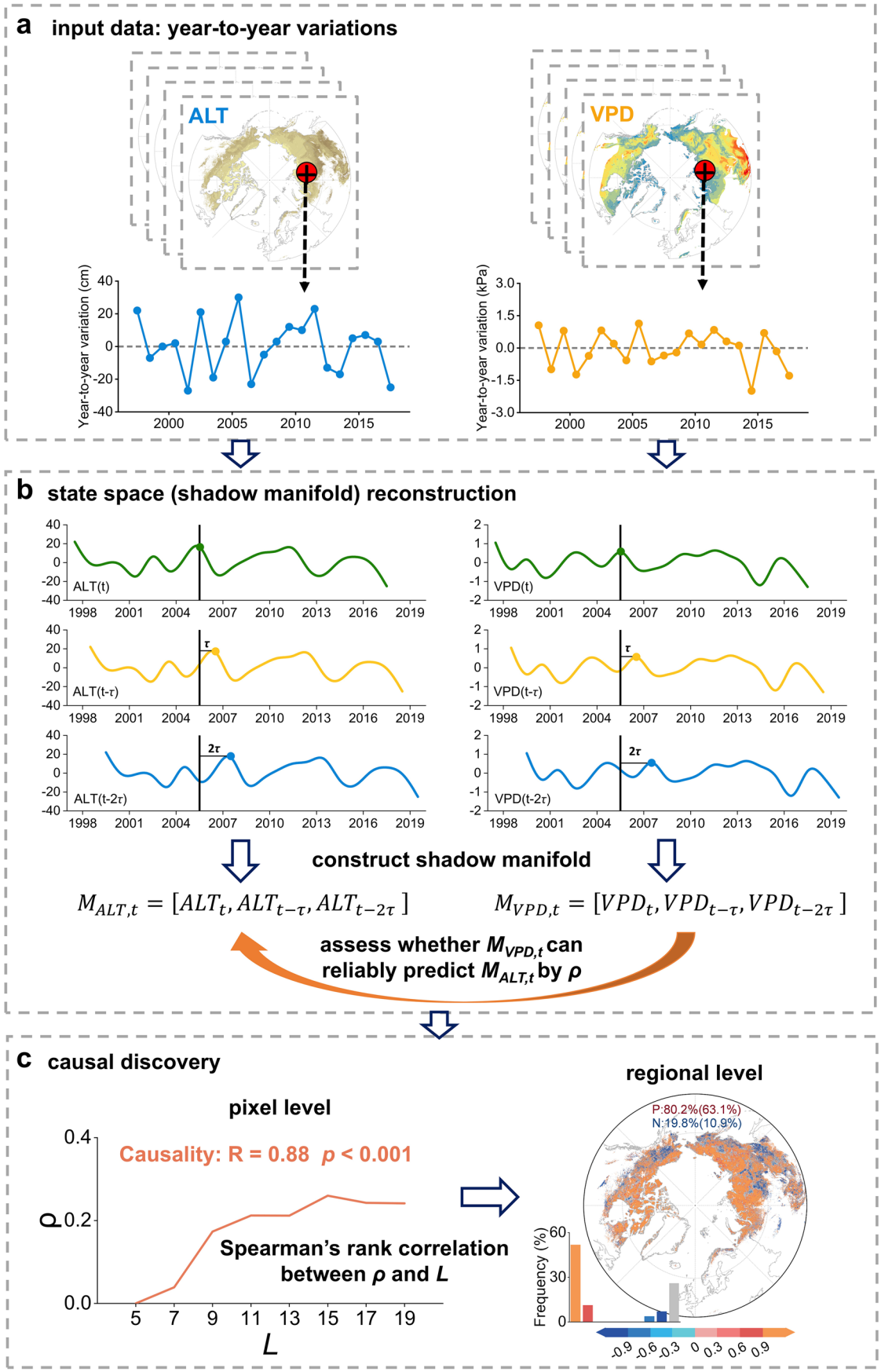

Extended Data Fig. 1 | See next page for caption.

https://doi.org/10.1038/s41561-025-01894-y

Extended Data Fig. 1 | Schematic of causal discovery using CCM model, illustrated with the example "ALT causes VPD". a, Year-to-year variations of ALT and VPD serve as inputs to the CCM model. **b**, The CCM model detects causality based on non-linear state space reconstruction. It first constructs shadow manifolds for ALT ($M_{ALT,t}$) and VPD ($M_{VPD,t}$) in a three-dimensional state space using the original (ALT(t); VPD(t)) and two time-lagged series (ALT(t-τ), ALT(t-2τ); VPD(t-τ), VPD(t-2τ)). Predict skill (ρ) is then used to assess whether $M_{VPD,t}$ can reliably predict the state of ALT. **c**, If ρ converges as the increase of time series length (L), it suggests that ALT causally influences VPD. This convergence is assessed by calculating Spearman's rank correlation between ρ and L, identifying causality only when the correlation is significantly positive (Methods). Maps created in ArcGIS (v.10.8) using a base map derived from the IPCC-WG1 Atlas GitHub repository[80].

https://doi.org/10.1038/s41561-025-01894-y

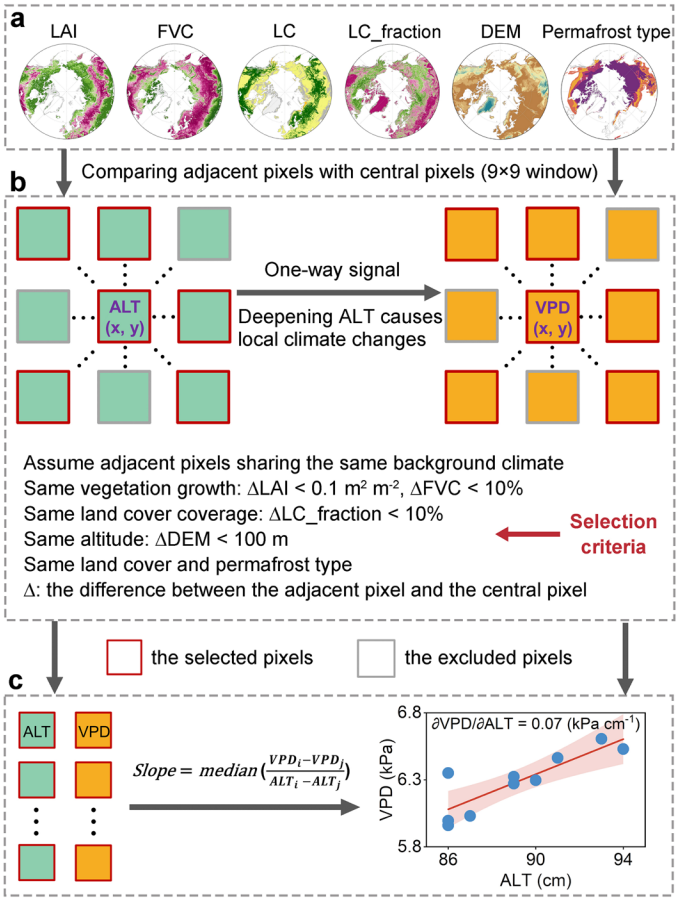

Extended Data Fig. 2 | Schematic of the space-for-time approach to derive the sensitivities of various climatic factors (for example, VPD) to the deepening ALT. This method assumes that the adjacent pixels share the same background climate with the central pixel within the spatial moving window (set as 9×9 pixels in our study). It can therefore detect the one-way signal representing the climatic feedback from the deepening ALT. **a-b**, Adjacent pixels were selected based on criteria that can exclude the confounding effects of vegetation dynamics (LAI and FVC), land-cover changes (main land-cover type, LC; fraction of main land-cover type, LC_fraction), topography (DEM), and permafrost type. **c**, Theil-Sen slope estimator was applied to estimate sensitivity by pooling all selected adjacent pixels and the central pixel itself together. This method was also used to estimate the sensitivities of vegetation growth (FVC and LAI) and below-ground fuel dryness (FFMC, DMC, and DC) to ALT. The constraints of vegetation dynamics on the selection of adjacent pixels were not considered when calculating the sensitivity of FVC and LAI to ALT. The shaded area in **c** indicates the 95% confidence interval of fitting line. Maps created in ArcGIS (v.10.8) using a base map derived from the IPCC-WG1 Atlas GitHub repository[80].

https://doi.org/10.1038/s41561-025-01894-y

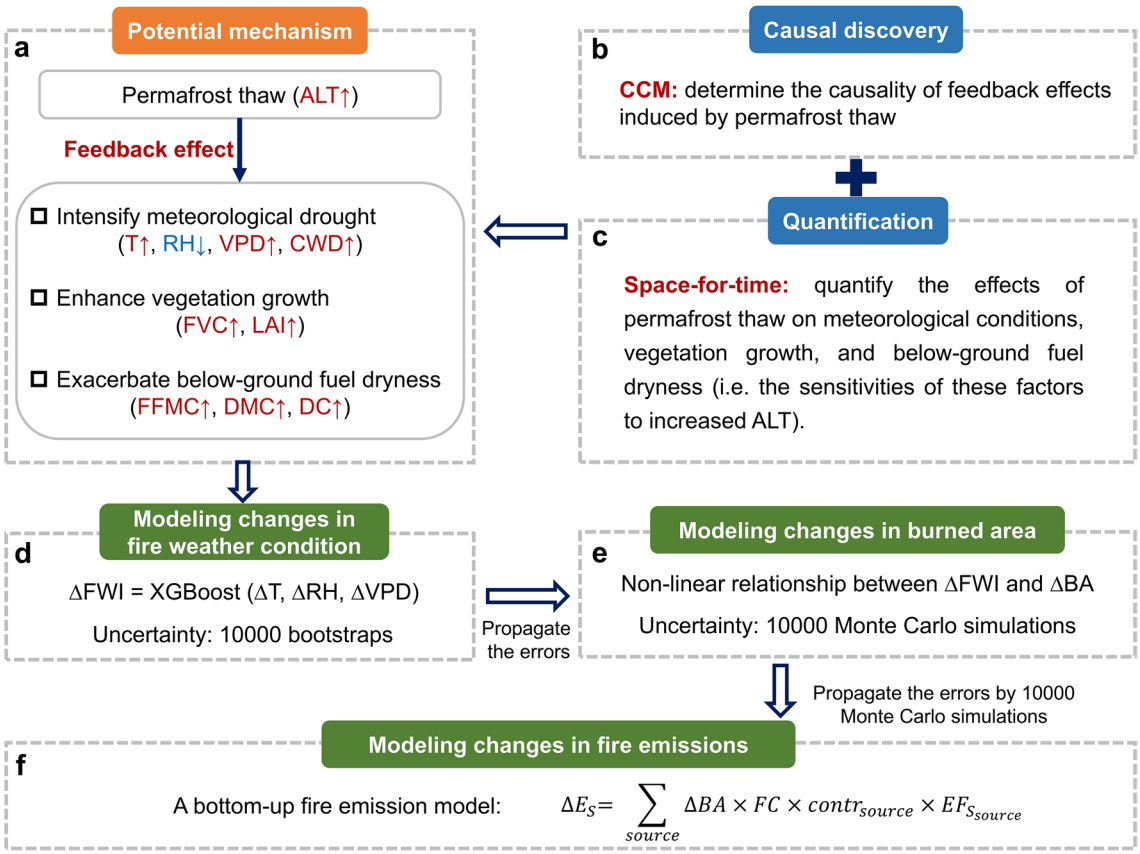

Extended Data Fig. 3 | A summary flowchart of the methodologies used in this study. a, Permafrost thaw amplifies Arctic–boreal fire regimes through three potential feedback effects: intensifying meteorological drought, enhancing vegetation growth, and exacerbated below-ground fuel dryness. To investigate these mechanisms, we employed CCM model to qualitatively assess causal relationships (**b**) and a space-for-time approach to quantificationally estimate the sensitivities of these factors to permafrost thaw (**c**). Subsequently, to provide a preliminary estimation of changes in fire regimes induced by permafrost thaw, we applied a XGBoost-based model to predict changes in fire weather conditions (**d**), a non-linear model to estimate changes in burned area (**e**), and a bottom-up model to calculate associated changes in fire emissions (**f**). Uncertainty propagation was incorporated throughout the estimation of changes in fire regimes using Monte Carlo simulations.

https://doi.org/10.1038/s41561-025-01894-y

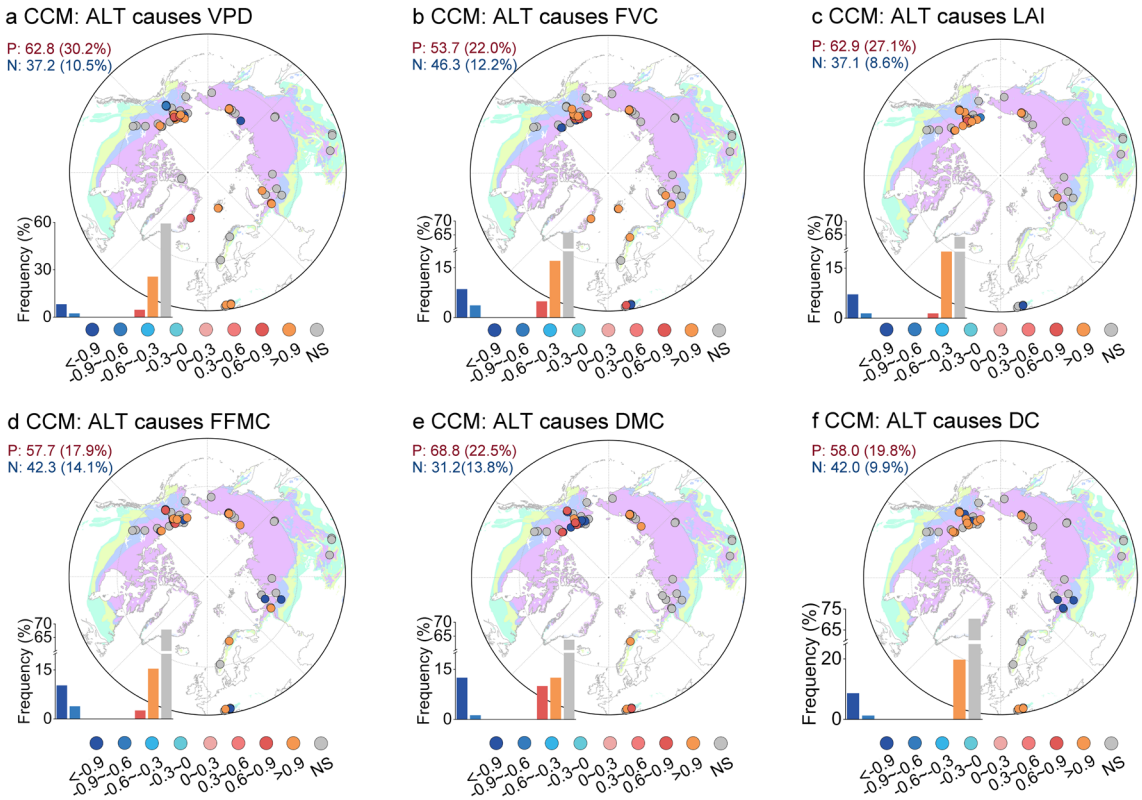

Extended Data Fig. 4 | Causal discovery by CCM model for the feedback effects of the deepening ALT on meteorological variable (VPD; a), vegetation growth (FVC and LAI; b and c), and below-ground fuel dryness (FFMC, DMC, and DC; d-f) based on ALT ground measurements from the CALM network. The maps display Spearman's rank correlation coefficients between predictive skill (ρ) and the length of the time series (L) estimated by the CCM model. The base map shows different permafrost types (continuous, discontinuous, isolated, and sporadic). P and N indicate the percentage of positive and negative correlations between ρ and L, respectively. Maps created in ArcGIS (v.10.8) using a base map derived from the Circum-Arctic Map of Permafrost and Ground-Ice Conditions (https://nsidc.org/data/GGD318/versions/2), the IPCC-WG1 Atlas GitHub repository[80] and our results[81].

https://doi.org/10.1038/s41561-025-01894-y

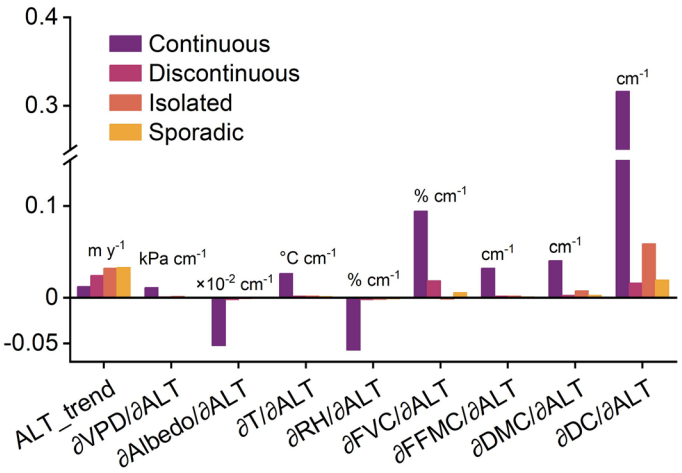

Extended Data Fig. 5 | Comparisons across different permafrost types (continuous, discontinuous, isolated, and sporadic). Bars indicate the regional means of the long-term ALT trend (ALT_trend) and the sensitivities of various variables (VPD, Albedo, T, RH, FVC, FFMC, DMC, and DC) to ALT.

https://doi.org/10.1038/s41561-025-01894-y

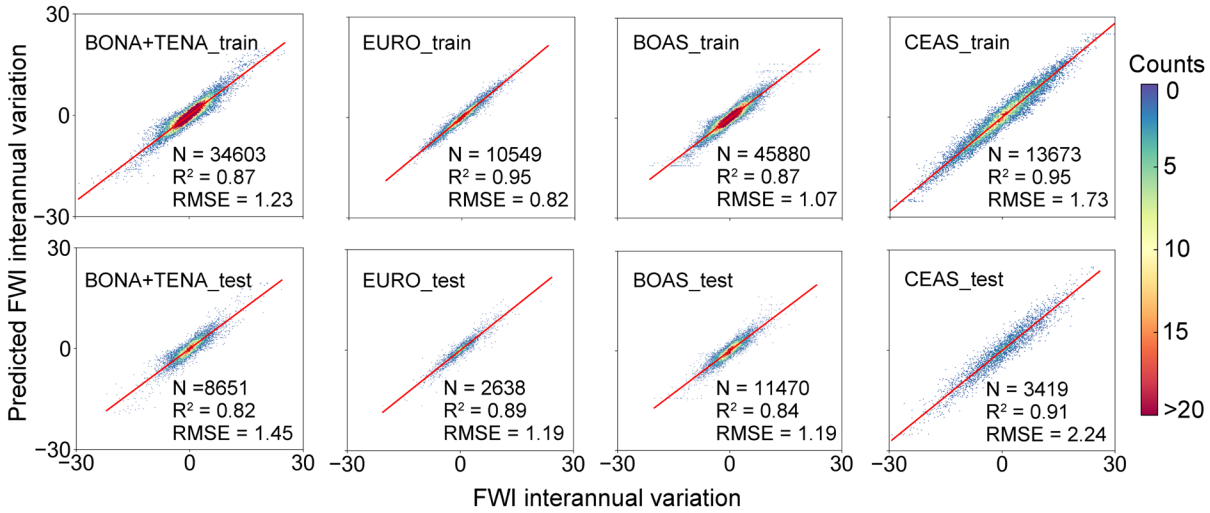

Extended Data Fig. 6 | Model accuracy of the XGBoost-based FWI models for the training and testing data sets across different GFED regions. Each subplot shows the scatter of predicted versus actual FWI interannual variation (that is, the difference between two consecutive years), with R^2 and RMSE indicating model performance. N indicates the sample sizes for the training and testing data sets. BONA, Boreal North America; TENA, Temperate North America; EURO, Europe; BOAS, Boreal Asia; CEAS, Central Asia. Since only a small portion of TENA lies above 45°N (Fig. S6), we combined BONA and TENA for training the XGBoost model.

https://doi.org/10.1038/s41561-025-01894-y

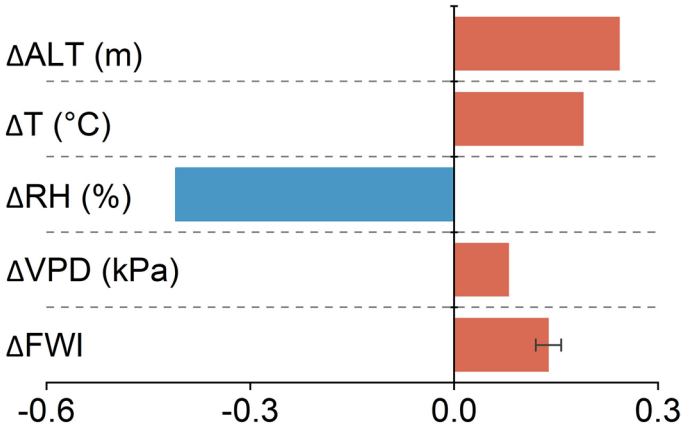

Extended Data Fig. 7 | Changes of active layer thickness (ΔALT) over 1997-2018 and their induced changes in summer air temperature (ΔT), relative humidity (ΔRH), vapor pressure deficit (ΔVPD), and fire weather index (ΔFWI) across the norther permafrost regions. Bars indicate regional averages. Bars and error bars for ΔFWI are presented as mean values ±1 standard deviation of regional average derived from 10000 bootstrapped XGBoost model runs.

https://doi.org/10.1038/s41561-025-01894-y

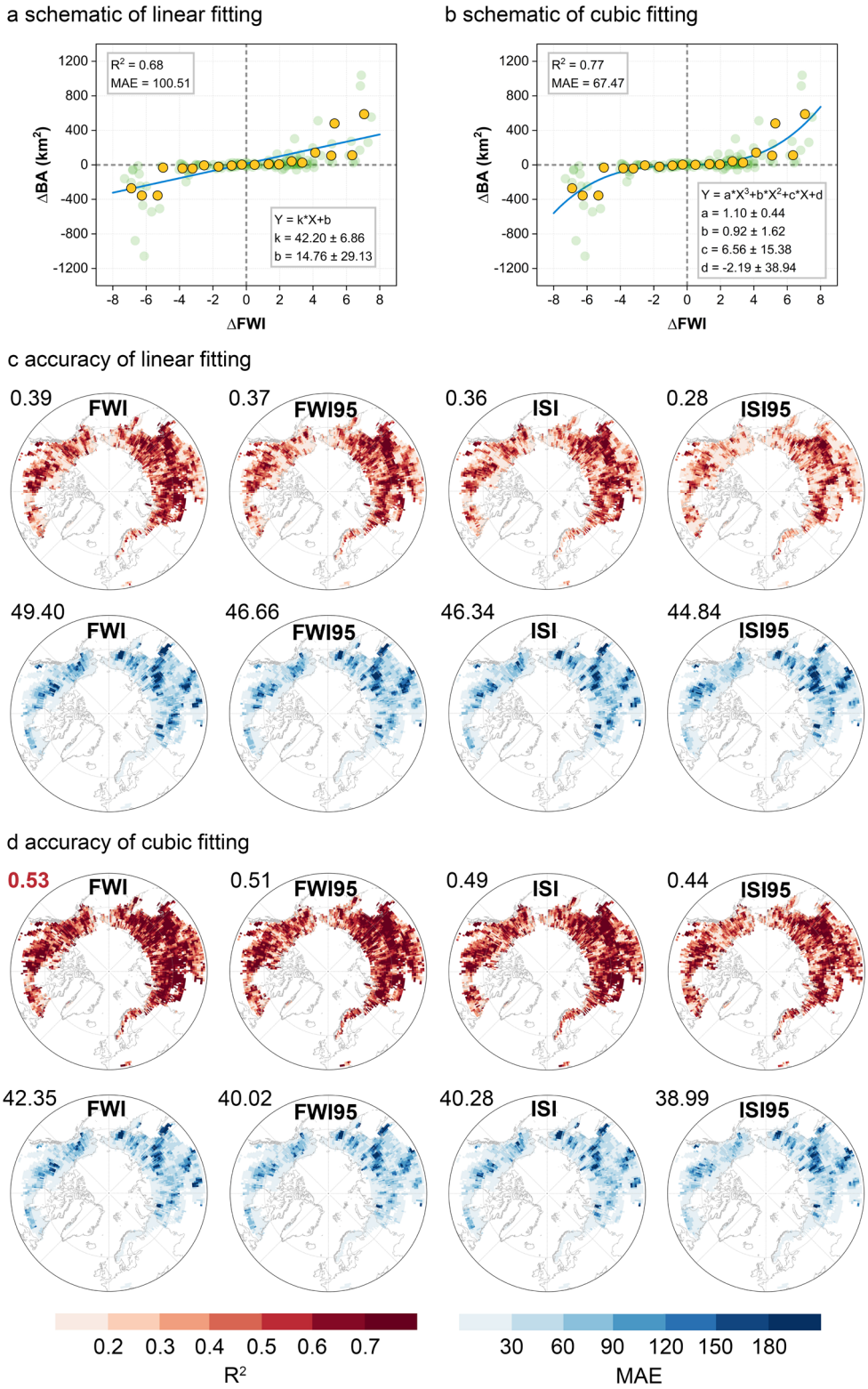

Extended Data Fig. 8 | Modeling the relationships between changes in summer total burned area (ΔBA) and changes in summer fire weather variables using linear and cubic functions. Fire weather variables include FWI and its annual 95th percentile (FWI_{95}), as well as ISI and its annual 95th percentile (ISI_{95}). **a-b**, Schematic of liner (**a**) and cubic fittings (**b**). R^2 and mean absolute error (MAE) were used to evaluate model performance. **Δ** indicates the year-to-year variation (that is, the difference between two consecutive years). The green circles include long time series data within a 3×3 spatial moving window. The yellow circles represent the mean **Δ**BA values under 20 bins of **Δ**FWI. The blue line indicates the fitted linear or cubic regression. **c-d**, Spatial patterns of model accuracy for the linear (**c**) and cubic models (**d**), with labels indicating regional average R^2 and MAE values. The cubic function was selected to model the relationship between **Δ**BA and **Δ**FWI, as it yielded the highest R^2 (0.53; red label). Maps created with ArcGIS (v.10.8) using basemap data from the IPCC-WG1 Atlas GitHub repository[80].

https://doi.org/10.1038/s41561-025-01894-y

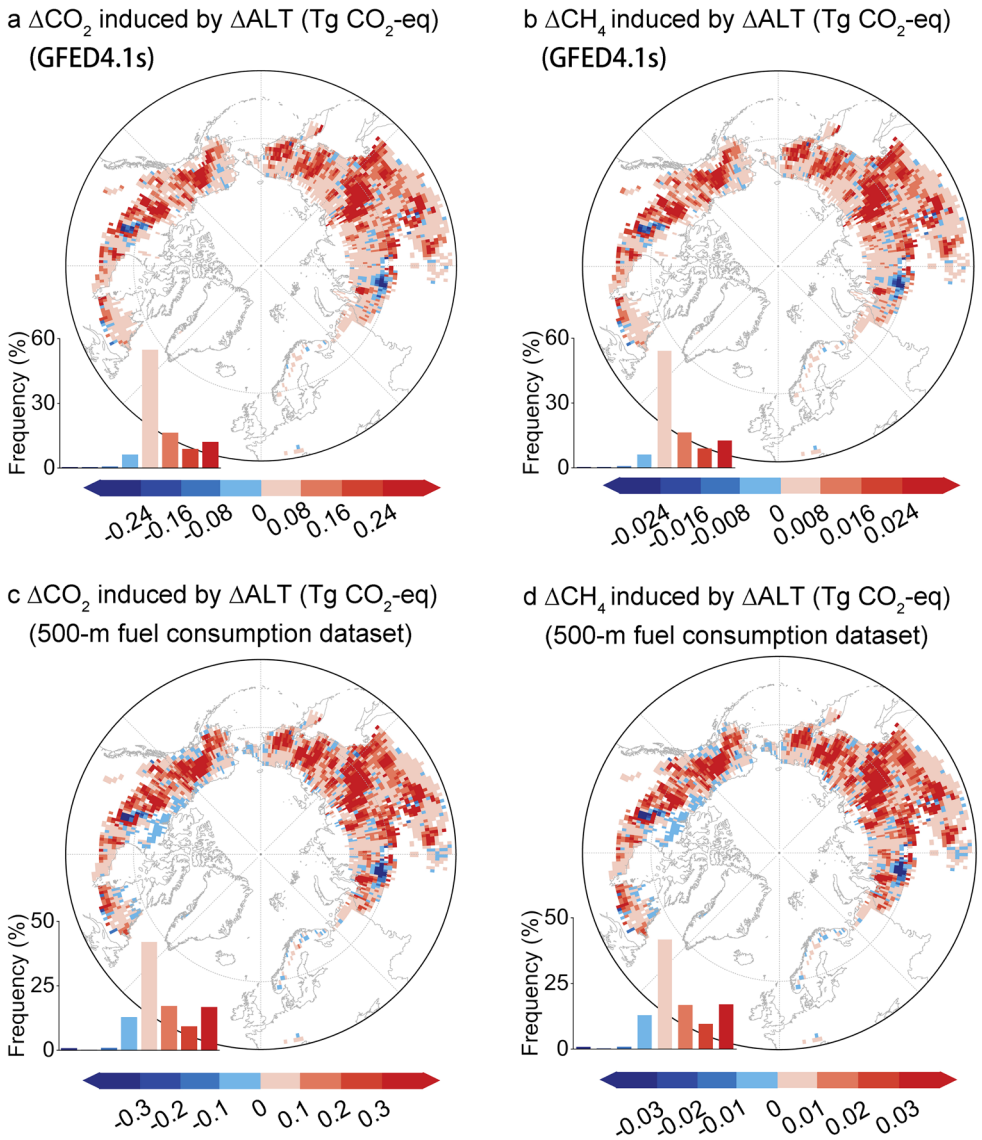

Extended Data Fig. 9 | Changes in CO_2 (ΔCO_2) and CH_4 (ΔCH_4) emissions from fire induced by the deepening active layer thickness (ΔALT) during 1997-2018. ΔCO_2 and ΔCH_4 induced by ΔALT based on the GFED4.1 s (**a-b**) and the 500-m fuel consumption (**c-d**) datasets. Emissions of CO_2 and CH_4 were estimated as the mean values from 10000 iterations of the Monte Carlo simulations, which consider the propagation of uncertainties in the emission estimates. Maps created with ArcGIS (v.10.8) using basemap data from the IPCC-WG1 Atlas GitHub repository[80].

https://doi.org/10.1038/s41561-025-01894-y

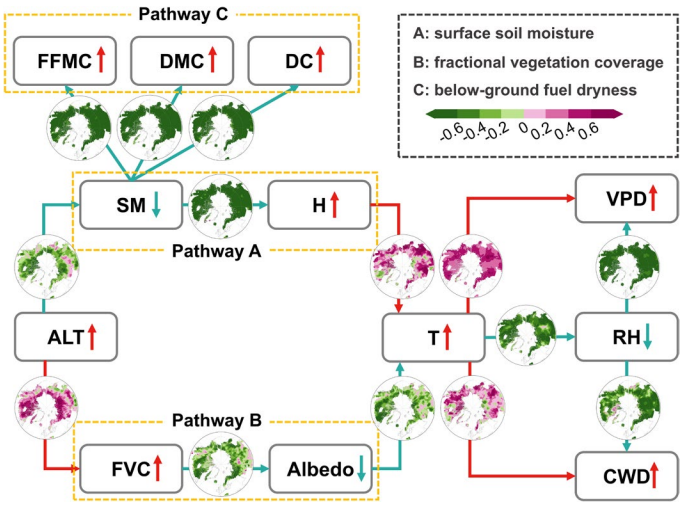

Extended Data Fig. 10 | A synthesis of the cascade linking deepening ALT, summer fire-prone meteorological conditions, above-ground vegetation growth, and below-ground fuel dryness, as analyzed using a structural equation model (SEM). Three pathways were designed to describe the feedback chains triggered by the deepening ALT and their interactions. Red arrows indicate positive path coefficients or increased effects, while green arrows indicate negative path coefficients or decreased effects. The SEM was conducted at the grid-cell level. Maps between connected variables show the spatial pattern of path coefficients across the Arctic-boreal region. FVC, fractional vegetation coverage; SM, surface soil moisture content; H: flux of surface sensible heat; T, air temperature; RH, relative humidity; VPD, vapor pressure deficit; CWD, climatic water deficit; FFMC, fine fuel moisture code; DMC, duff moisture code; DC, drought code. Maps created with ArcGIS (v.10.8) using basemap data from the IPCC-WG1 Atlas GitHub repository[80].